Development/Plasticity/Repair

Loss of RNA-Binding Protein HuR Leads to Defective Ependymal Cells and Hydrocephalus

Xiu Han,[1,2] Xuning Shen,[1,2] Min Wang,[1] Xin Wang,[3] Youli Jian,[1] Chonglin Yang,[3] and Weixiang Guo[1,2]

[1]State Key Laboratory for Molecular and Developmental Biology, Institute of Genetics and Developmental Biology, Chinese Academy of Sciences, Beijing 100101, China, [2]Graduate School, University of Chinese Academy of Sciences, Beijing 100093, China, and [3]State Key Laboratory of Natural Resource Conservation and Utilization in Yunnan, Center for Life Science, School of Life Sciences, Yunnan University, Kunming 650021, China

Multiciliated ependymal cells line the ventricle wall and generate CSF flow through ciliary beating. Defects in ependymal cells cause hydrocephalus; however, there are still significant gaps in our understanding the molecular, cellular and developmental mechanisms involved in the pathogenesis of hydrocephalus. Here, we demonstrate that specific deletion of RNA-binding protein (RBP) Hu antigen R (HuR) in the mouse brain results in hydrocephalus and causes postnatal death. HuR deficiency leads to impaired ependymal cell development with defective motile ciliogenesis in both female and male mice. Transcriptome-wide analysis reveals that HuR binds to mRNA transcripts related to ciliogenesis, including cilia and flagella associated protein 52 (*Cfap52*), the effector gene of Foxj-1 and Rfx transcriptional factors. HuR deficiency accelerates the degradation of *Cfap52* mRNA, while overexpression of Cfap52 is able to promote the development of HuR-deficient ependymal cells. Taken together, our results unravel the important role of HuR in posttranscriptional regulation of ependymal cell development by stabilizing *Cfap52* mRNA.

Key words: ependymal cell; HuR; hydrocephalus

Significance Statement

This study identifies Hu antigen R (HuR) as a genetic factor involved in the pathogenesis of hydrocephalus. Mechanistically, HuR regulates ependymal cell differentiation and ciliogenesis through stabilizing *Cfap52* mRNA, the effector gene of Foxj-1 and Rfx transcriptional factors.

Introduction

Hydrocephalus, estimated to affect 1 in 1000 infants, is caused by abnormal CSF flow, leading to progressive ventricular dilatation and brain damage (Tully and Dobyns, 2014; Kahle et al., 2016). Most infantile hydrocephalus cases are congenital, which is particularly difficult to treat and often result in the severe neurologic outcomes with high mortality (Kahle et al., 2016). The most common therapeutic intervention is surgical insertion of a catheter to drain excess CSF into another body cavity. However, this intervention only reverses 10–20% of the neurologic impairment of neonates with fetal onset hydrocephalus, suggesting that hydrocephalus may not only be a disorder of CSF dynamic but also a brain disorder (Guerra et al., 2015). Based on the CSF

dynamics, hydrocephalus is classified as obstructive, resulting from impeded CSF circulation, or nonobstructive, caused by increased CSF production or impaired CSF resorption (Kahle et al., 2016; Kousi and Katsanis, 2016). Although obstruction of CSF is the most common cause in congenital hydrocephalus (McAllister, 2012; Tully and Dobyns, 2014), the underlying cellular and molecular mechanisms are not well understood yet.

The multiciliated ependymal cells lining the ventricular wall are derived from radial glia cells (RGCs) and fully differentiated during postnatal development (Spassky et al., 2005; Spassky and Meunier, 2017). The cilia are nucleated from microtubule-based basal bodies (BBs; Marshall, 2008) and coordinated beating of cilia on the apical surface of ependymal cells generates unidirectional CSF flow (Del Bigio, 2010). Moreover, ependymal cells exhibit two forms of planar cell polarity (PCP; Mirzadeh et al., 2010b): translational polarity, the asymmetric positioning of the cluster of BB (BB patch) on the apical surface of the cell, and rotational polarity, the unidirectional orientation of individual BB within each cell. Coordinated ciliary beating and parallel ciliary bundles are derived from the translational and rotational polarity of planar polarized BB in ependymal cells (Spassky and Meunier, 2017). Disruptions to differentiation, ciliogenesis and/or planar polarity of ependymal cells result in an accumulation

of CSF in the brain ventricles and ultimately lead to hydrocephalus (Marshall, 2008; Del Bigio, 2010; Spassky and Meunier, 2017), but the mechanisms underlying regulation of these cellular processes in ependymal cells remain unclear.

Posttranscriptional regulation by RNA-binding proteins (RBPs), an essential mechanism for controlling gene expression, plays important roles in all aspects of brain development (Pilaz and Silver, 2015). Hu antigen R [HuR; also known as embryonic lethal, abnormal vision-like 1 (ELAVL1)] belongs to the highly conserved ELAV/Hu family of RBP (Yao et al., 1993). HuR is ubiquitously expressed and shuttled between the cytoplasm and nucleus via its hinge region (Fan and Steitz, 1998). HuR is not only involved in stabilizing or modulating translation of numerous target mRNAs in cytoplasm, but also in assisting with alternative splicing and nuclear processing of its target transcripts in nucleus (Srikantan and Gorospe, 2011). Our previous study demonstrates that ablation of HuR in NSCs impairs adult but not embryonic neurogenesis (Wang et al., 2019). However, the role of HuR in postnatal brain development is still unknown.

In this study, we show that specific deletion of HuR in the brain results in postnatal congenital hydrocephalus. In HuR-deficient mice, ependymal cell development is compromised, leading to defective CSF dynamics. Mechanistically, HuR stabilizes its targeted mRNA transcript, *Cfap52*, which is required for the development of ependymal cells. Therefore, HuR deficiency leads to defective posttranscriptional regulation of ependymal cell development, which contributes to the pathogenesis of congenital hydrocephalus.

Materials and Methods

Animals
All mice were maintained with a 12/12 h light/dark cycle and provided with food and water *ad libitum* in the animal facility at Institute of Genetics and Developmental Biology, Chinese Academy of Sciences. All procedures and husbandry were performed according to protocols approved by the Institutional Animal Care and Use Committee at Institute of Genetics and Developmental Biology, Chinese Academy of Sciences. HuR conditional knock-out mouse (cKO) line was generated by crossing *HuR$^{flox/flox}$* mouse (Ghosh et al., 2009) with Nestin-Cre driver mouse (Zimmerman et al., 1994). No significant phenotypic differences were detected between male and female mice, both genders thus were included in the analysis.

For bromodeoxyuridine (BrdU) experiments, timed-pregnant mice were injected intraperitoneally with BrdU (200 mg/kg, Sigma-Aldrich, B5002) and analyzed at appropriate time.

Histology and immunohistochemistry
Embryonic mouse brains were extracted at appropriate ages and fixed with 4% paraformaldehyde (PFA). Postnatal mouse were euthanized by intraperitoneal injection of Avertin. The brains were extracted after transcardial perfusion with 4% PFA, postfixed with 4% PFA at 4°C overnight, and rinsed with PBS.

For preparation of paraffin-embedded sections, the fixed brains were dehydrated with ethanol, embedded in paraffin blocks, and cut at 10-μm thickness. Areas of ventricles and choroid plexus were measured using the NIS-Elements, BR. 3.00 software (Nikon).

For preparation of cryo-sections, the fixed brains were incubated in 30% sucrose overnight, immersed in O.C.T. compound (SAKURA 4583), frozen at −80°C overnight, and sectioned at 20-μm thickness. The cyro-sections were washed with PBS and blocked with 3% normal donkey serum and 0.3% Triton X-100 for 1 h at room temperature. After overnight incubation with primary antibodies diluted in the blocking solution with gentle agitation at 4°C, sections were washed and incubated with appropriate Alexa Fluor-conjugated secondary antibodies at room temperature for 2 h. All sections were counterstained with a nuclear counter stain, 4′,6-dimidino-2′-phenylindole dihydrochloride (DAPI; Sigma-Aldrich, #B2261).
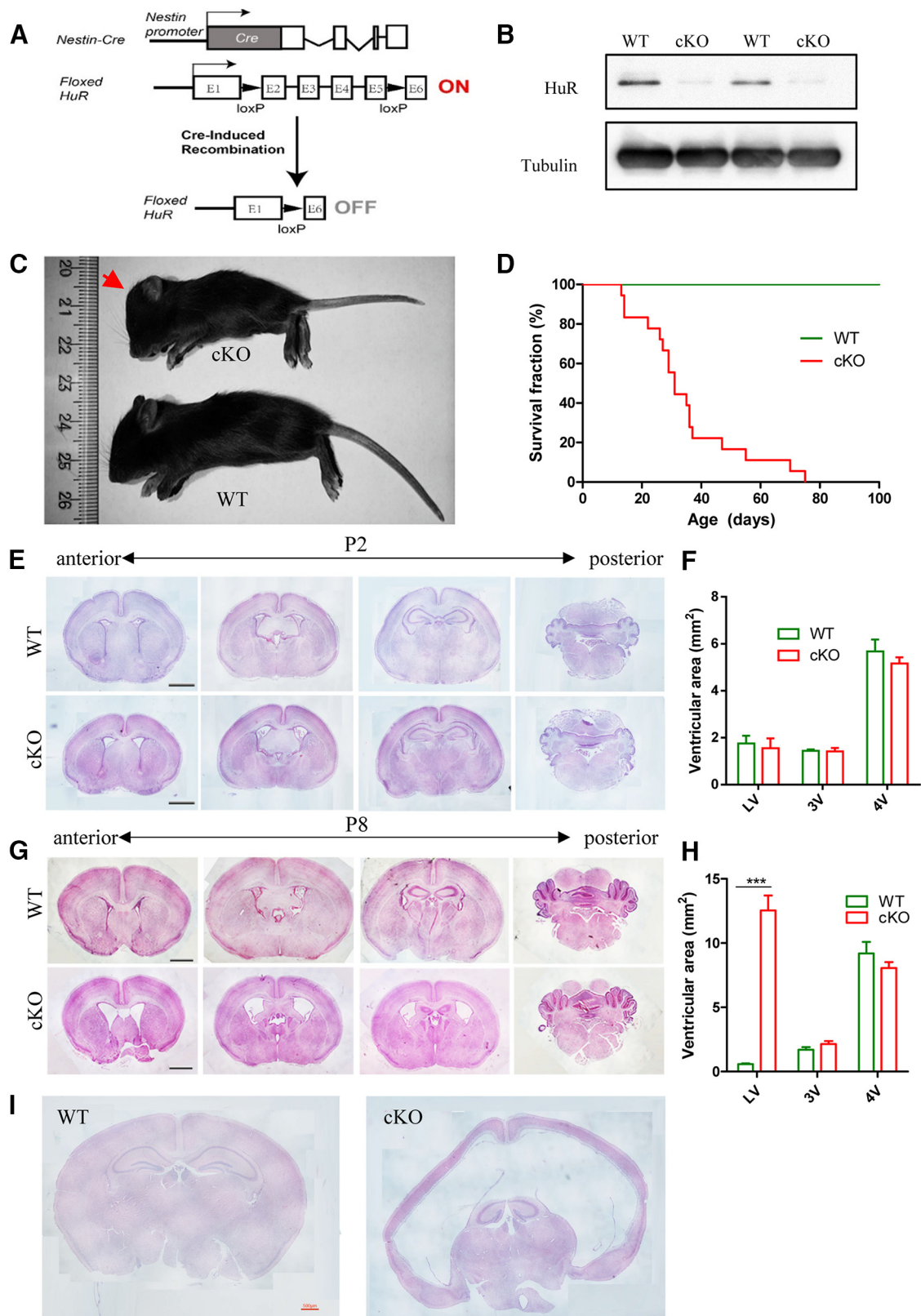
Whole-mounts of the lateral ventricle (LV) walls were prepared as described previously (Mirzadeh et al., 2010a). The exposed LV walls were fixed in 4% PFA at 4°C overnight. After blocking with 3% normal donkey serum and 0.3% Triton X-100, whole-mounts were incubated with primary antibodies in the blocking solution overnight at 4°C, washed, and incubated with secondary antibodies in the blocking solution overnight at 4°C.

The following primary antibodies were used: mouse anti-acetylated tubulin (1:1000, Sigma T6793), mouse anti-E-cadherin (1:500, BD Transduction Laboratories, 610181), goat anti-orthodenticle homeobox 2 (Otx2; 1:1000, R&D, AF1979), rabbit anti-centrosomal protein 164 (CEP164; 1:200, Abcam ab221447), rabbit anti-β-catenin (1:500, Sigma, C2206), rat anti-CD24 conjugated with PE (1:100, BD Pharmingenin, 553262), rabbit anti-S100β (1:1000, Dako, Z0311), mouse anti-γ-tubulin (1:1000, Abcam, ab11316), rabbit anti-Na-K-ATPase (1:200, Abcam, ab76020), goat anti-Sox2 (1:200, Santa Cruz, sc-17 320), mouse anti-Satb2 (1:500, Abcam, ab51502), rat anti-Ctip2 (1:500, Abcam, ab18465), goat anti-Cux1 (1:500, Santa Cruz, sc-13024), rabbit anti-Ki67 (1:200, Thermofisher, 9106), rabbit anti-Tbr1 (1:500, Abcam ab31940), chicken anti-Tbr2 (1:500, Certificate of Analysis, AB15894), rabbit anti-Pax6 (1:500, Biolegend, 901301), mouse anti-BrdU (1:1000, Abcam, ab6362), mouse anti-HuR (1:1000, Abcam, ab136542), and anti-Cfap52 (1:500, CUSABIO, CSB-PA839781LA01HU). Alexa Fluor-conjugated secondary antibodies (Alexa Fluor 488, 594, or 647, Abcam, 1:1000) were used.

The images were taken on a LSM700 laser confocal microscope (Carl Zeiss). To analyze BB patch angle and BB rotational orientation, the vectors were drawn using the ImageJ software (National Institutes of Health). The angles of the vectors were normalized so that the average of the angle of the vectors is 180° in each ependymal cell. The percentage of vectors were plotted on a histogram in 15° bins. BB displacement was quantified using the ImageJ software.

Electron microscopy
Mouse were perfused with 4% PFA/1% glutaraldehyde in 0.1 M sodium cacodylate buffer. For transmission electron microscopy, the tissues with the LV walls were pos-fixed with 2.5% glutaraldehyde (electron microscopy sciences; EMS) in phosphate buffer (PB) at 4°C for overnight, washed with PBS, postfixed with 2% osmium (EMS) in PB for 2 h at RT, rinsed with PBS, stained with 2% uranyl acetate (EMS) in 70% ethanol at 4°C for 2.5 h, dehydrated with ethanol, incubated in propylene oxide (EMS), and embedded in Durcupan resin Fluka (Sigma-Aldrich). Tissues were sectioned (80-nm thickness) with an EM UC6

Table 1. Oligonucleotides in this study

qPCR primers	Sequence
Rfx3 forward	GTGACAGGAGAGACACCGAT
Rfx3 reverse	ACAGCACTCTCCAGAACAGG
Foxj1 forward	CAACTTCTGCTACTTCCGCC
Foxj1 reverse	TTCTTGAAGGCCCCACTGAG
Cfap52 forward	AGGAAGGAGGGCACTTTGTT
Cfap52 reverse	TGCGCTCACACTGACGATAT
Spef2 forward	TTGGCTTCTTGGACAACTGG
Spef2 reverse	GAAGAAAGGGGAGGGCTCAT
luciferase-control RNA forward	AAGAGATACGCCCTGGTTCC
luciferase-control RNA reverse	CCGATAAATAACGCGCCCAA
18s forward	AATCAGGGTTCGATTCCGGA
18s reverse	CCAAGATCCAACTACGAGCT
Genotyping primers	
HuRf/f forward	CTCTCCAGGCAGATGAGCA
HuRf/f reverse	TAGGCTCTGGGATGAAACCT
Nestin::Cre forward	CGATGCAACGAGTGATGAGG
Nestin::Cre reverse	CGCATAACCAGTGAAACAGC
Target sequences of the shRNA	
Cfap52 shRNA	GCCATGGCATTGACTTCATGA
Spef2 shRNA	GCCAAGAAGGAGAAAGAAGCA

Figure 1. HuR deficiency leads to progressive postnatal hydrocephalus. ***A***, Schematic drawing of the conditional HuR gene targeting strategy. ***B***, Western blot to detect HuR protein in brain lysates of WT and cKO mice. ***C***, Photograph showing WT and cKO mice at P28. The arrow indicates the dome-shaped head in a cKO mouse. ***D***, Survival analysis of WT and cKO mice. WT: $n = 10$ mice; cKO: $n = 18$ mice. ***E***, H&E staining of paraffin-embedded coronal sections of WT and cKO mouse brain at P2. Scale bar: 1 mm. ***F***, Quantification of the ventricle area between WT and cKO mouse brain at P2. WT, $n = 3$ mice; cKO, $n = 3$ mice. ***G***, H&E staining of paraffin-embedded coronal sections of WT and cKO mouse brain at P8. Scale bar: 1 mm. ***H***, Quantification of the ventricle area between WT and cKO mouse brain at P8. LV: WT, $n = 3$ mice; cKO, $n = 4$ mice; 3V: WT, $n = 3$ mice; cKO, $n = 4$ mice; 4V: WT, $n = 4$ mice; cKO, $n = 3$ mice. ***I***, H&E staining of paraffin-embedded coronal sections of WT and cKO mouse brain at P18. Scale bar: 500 μm. Data are presented as mean $\pm$ SEM; $\ast\ast\ast p < 0.001$. LV, lateral ventricle; 3V, third ventricle; 4V, fourth ventricle.
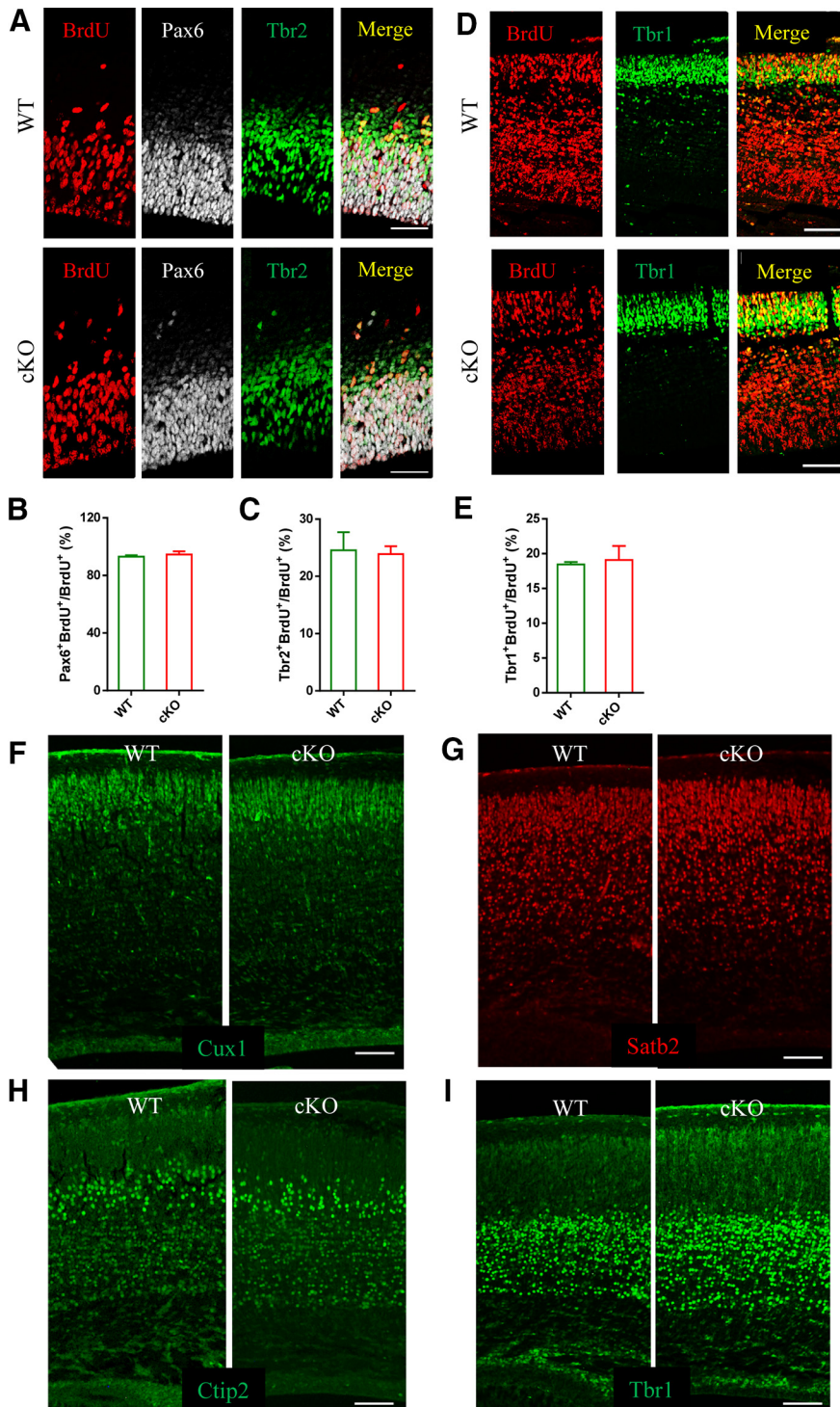
Figure 2. HuR deficiency does not affect embryonic neurogenesis and neuronal patterning during embryonic brain development. *A*, Sample images of E14.5 brain sections stained with BrdU, Pax6, and Tbr2 after 2 h BrdU injection. Scale bars: 50 μm. *B*, *C*, Quantification of BrdU$^+$Pax6$^+$ cells (*B*, $p = 0.61$) and BrdU$^+$Tbr2$^+$ cells (*C*, $p = 0.83$) in E14.5 cerebral cortex of WT and cKO mice. WT, $n = 3$ mice, cKO, $n = 4$ mice. Data are presented as mean ± SEM. *D*, Sample images of E16.5 brain sections stained with BrdU and Tbr1 after 48 h BrdU injection at E14.5. Scale bars: 100 μm. *E*, Quantification of BrdU$^+$Tbr1$^+$ cells in E16.5 cerebral cortex of WT and cKO mice ($p = 0.73$). WT, $n = 4$ mice, cKO, $n = 3$ mice. *F–I*, Sample images of P0 WT and cKO brain sections stained with Cux1 (*F*), Satb2 (*G*), Ctip3 (*H*), and Tbr1 (*I*). Scale bar: 100 μm. Data are presented as mean ± SEM.

through a graded ethanol series, the sections were dried in a LEICA EM CPD300 critical point dryer. Dried specimens were then coated with gold in HITACHI E-1010 Auto sputter coater and viewed in a HITACHI S-3000N&Quorum PP3000T scanning electron microscope.

Ependymal flow assay and high-speed live imaging of ciliary beating
For the ependymal flow assay, the whole-mount preparation with LV wall was immobilized in a dish containing L-15 (Invitrogen, SH30525.01) medium. Fluorescent microbeads (2 μm, Polysciences) were deposited on the LV surface using a glass micropipette attached to a micromanipulator (NARISHIGE). The movement of the microbeads was recorded with 20-ms exposure time at 8 fps using a stereo microscope (LEICA M205 FA).

For high-speed imaging of ciliary beating, the whole-mount preparations with LV wall were incubated with rat anti-CD24 antibody conjugated with PE (1:100, BD Pharmingenin 553262) in Neurobasal medium (Invitrogen, 21103049) supplemented with B-27 serum-free supplement (Invitrogen, 17504-044), glutamine (Invitrogen, 25030-081), and antibiotics (Invitrogen, 15240-062) for 20 min at room temperature, rinsed with L-15 medium, and placed in a confocal dish with low melting point agarose (1–2%; Aladdin, A104063) and neurobasal medium with the supplements were placed on the whole-mounts. Ciliary beating was recorded with 30-ms exposure time at 5.5 fps for 200–250 frames at room temperature using a Zeiss Axio Observer Z1 microscope, Plan-Apochromat 40×/0.95 Korr M27, 1.2-×EMCCD Camera Adapter.

Primary culture of ependymal cells
Ependymal cell used in this study were isolated from lateral walls of LV of postnatal day (P)0 mice based on published method (Delgehyr et al., 2015). Briefly, dissociated cells from the brains were seeded in laminin-coated plate and maintained in DMEM (Corning 10-013-CVR) with 10% fetal bovine serum (FBS; Invitrogen, 10099-141c). When reached ~80% confluence after 5–7 d of culture, cells were rinsed with PBS, trypsinized, and seeded in poly-lysine and laminin-coated plate and maintained in DMEM with 10% FBS for a day. Then the medium was changed to DMEM without serum to induce cell differentiation. After 6–8 d of differentiation, cells were used for experiments.

Recombinant lentivirus production
Lentivirus production was performed as described previously (Tang et al., 2019). Briefly, lentiviral transfer vector DNA and packaging plasmid DNA were co-transfected into 293T cells. The medium was collected and pooled at 40, 64, and 88 h, and then filtered through a 0.2-μm filter. Viruses were concentrated by ultracentrifuge at 19,000 rpm

ultramicrotome (LEICA) and counterstained with uranyl acetate and lead citrate (EMS). For scanning electron microscopy, whole-mount preparations of LV were postfixed for overnight with 2.5% glutaraldehyde in PB, and kept in 1% osmium tetroxide. After dehydration for 2 h at 20°C using a SW27 rotor (Beckman). The viruses were washed once with PBS and then re-suspended in 150 μl PBS.
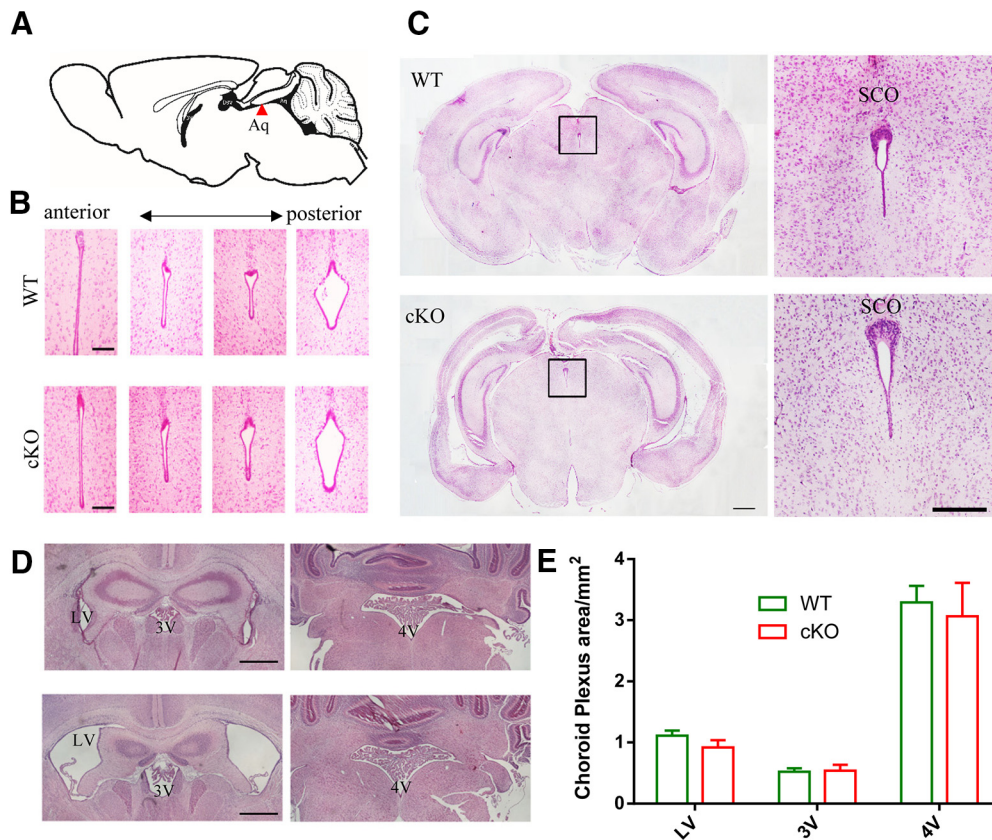
Figure 3. Anatomical analysis of the sylvian aqueduct, SCO, and choroid plexus in WT and cKO mice. ***A***, Schematic drawing of sagittal section of mouse brain. The arrowhead indicates the sylvian aqueduct (Aq). ***B***, Paraffin-embedded coronal sections stained with H&E to show the sylvian aqueduct of WT and cKO mice at P8, 100-mm intervals from anterior (left) to posterior (right). Stenosis was not observed in any section in cKO mice. Scale bar: 100 μm. ***C***, Paraffin-embedded coronal sections stained with H&E in WT and cKO mice at P14. Scale bar: 1 mm. The high magnifications of inset boxes in the left panel are showing the SCO structure of WT and cKO mice. Scale bar: 500 μm. ***D***, Paraffin-embedded sections stained with H&E, including the choroid plexus in LV, 3V, and 4V in the WT and cKO mice at P8. Scale bar: 500 μm. ***E***, Quantification of the area of the choroid plexus in the WT and cKO mice (LV $p = 0.26$, 3V $p = 0.89$, 4V $p = 0.72$). LV: WT, $n = 3$ mice, cKO, $n = 3$ mice; 3V: WT, $n = 3$ mice, cKO, $n = 4$ mice; 4V: WT, $n = 3$ mice, cKO, $n = 3$ mice. Data shown are presented as means ± SEM. LV, lateral ventricle; 3V, third ventricle; 4V, fourth ventricle.

RNA sequencing (RNA-seq) analysis

Total RNA was extracted from wild-type (WT) and cKO ependymal cells using TRIzol (Invitrogen). The integrity of the extracted total RNA was analyzed using Agilent 2100 Bioanalyzer (Agilent Technologies). The samples with RNA integrity number (RIN) ≥ 7 were subjected to the subsequent analysis. The libraries were constructed using TruSeq Stranded mRNA LTSample Prep kit (Illumina) according to the manufacturer's instructions. The standard Illumina protocol was used to prepare the libraries for RNA-seq. RNA-seq was performed using Illumina HiSeq2500 > 45 million 2 × 100 reads per sample was produced and alignment was performed using mouse genome database GRCm38 version 67. Only uniquely and properly mapped read pairs were used for further analysis. FPKM value of each gene was calculated using cufflinks, and the read counts of each gene were obtained by htseq-count. Differentially expressed genes (DEGs) were identified using the DESeq (2012) functions estimate Size Factors and nbinom test; $p < 0.05$ and fold change >0.2 were set as the threshold for significantly differential expression. Hierarchical cluster analysis of DEGs was performed to explore genes expression pattern. Gene ontology (GO) enrichment and KEGG pathway enrichment analysis of DEGs were, respectively, performed using R based on the hypergeometric distribution.

RNA immunoprecipitation

Cultured ependymal cells (2×10^7) were harvested and homogenized in 2 ml of ice-cold lysis buffer (10 mM HEPES, pH 7.4, 200 mM NaCl, 30 mM EDTA, and 0.5% Triton X-100) with 2× complete protease inhibitors (Roche, 11697498001) and 400 U/ml RNase inhibition (Promega,

N2511). Nuclei and debris were pelleted at 3000 × g for 10 min; the supernatant was collected and raised to 300 mM NaCl and clarified at 14,000 × g for 30 min. The resulting supernatant was precleared for 1 h with protein G agarose (GE Healthcare, 17-0618-01). An aliquot of precleared input was saved for RNA extraction (200 μl) and protein analysis (100 μl). An antibody against HuR (Abcam, ab136542.) was incubated with protein G agarose at 4°C for 2 h and washed three times with lysis buffer. RNase Inhibitors was added to the remaining lysates. The precleared lysates were immunoprecipitated with antibody-coated recombinant protein G agarose at 4°C overnight. After wash with the lyses buffer, 10% of immunoprecipitate was saved for protein analysis. The remaining was washed one more time and the immunoprecipitate was re-suspended into TRIzol (Invitrogen, 15596-018) for RNA isolation and followed by q-PCR or RNA-seq analysis.

RNA degradation assay

Total RNA was extracted from WT and cKO ependymal cells at 0 and 5 h after actinomycin D (MedChemExpress, HY-17559) treatment at a concentration of 5 mM. The standard Illumina protocol was used to prepare the libraries for RNA-seq. RNA-seq was performed using Illumina HiSeq2500 > 45 million 2 × 100 reads per sample was produced and alignment was performed using mouse genome database GRCm38 version 67. Fold changes at 5 h were normalized by fold changes at 0 h (no actinomycin D treatment) to specifically identify genes that degrade at a different slower rate in the cKO compared with WT, regardless of baseline changes in gene expression between two conditions. Genes with a normalized fold change lower than 0.2 in cKO over WT at 5 h were considered to be differentially degraded (Extended Data Fig. 12-3).
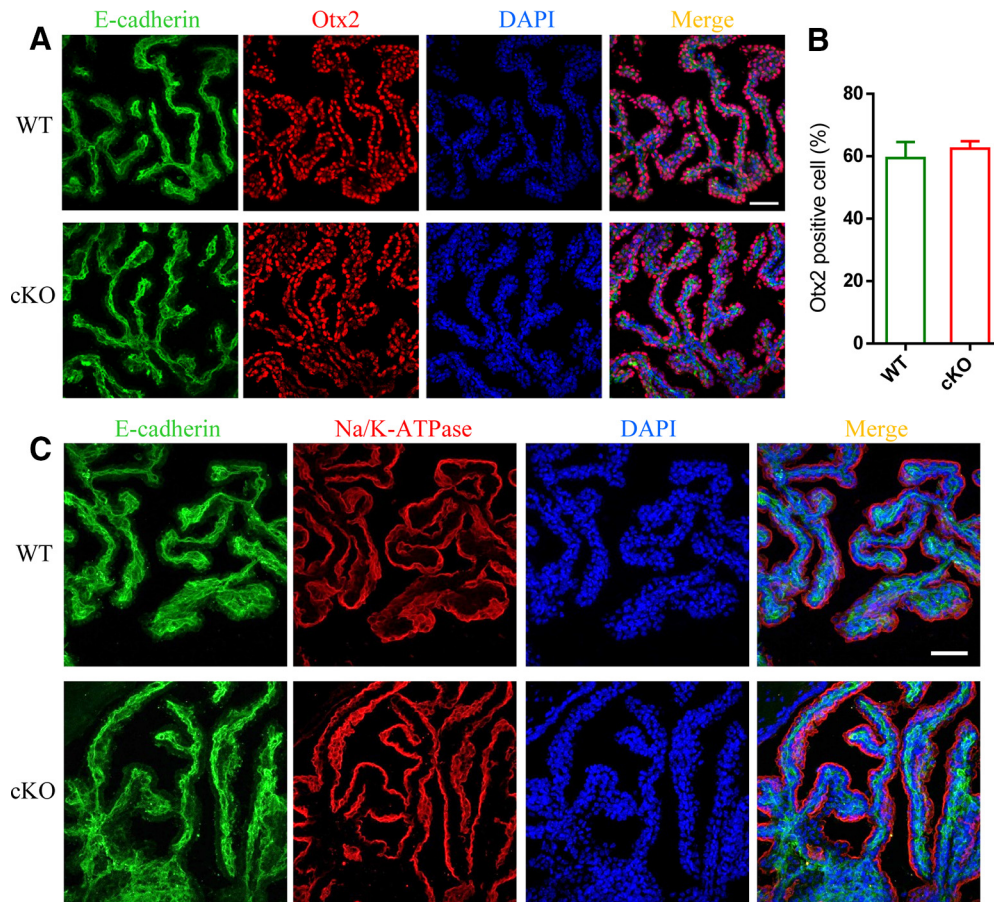
Figure 4. The differentiation of choroid plexus in WT and cKO mice. **A**, Sample images of the choroid plexus stained with E-cadherin and Otx2 in WT and cKO mice at P8. Scale bar: 50 μm. **B**, Percentages of Otx2$^+$ cells were quantified ($p = 0.62$). WT, $n = 3$ mice; cKO, $n = 3$ mice. Data are presented as mean $\pm$ SEM. **C**, Sample images of the choroid plexus stained with E-cadherin and Na/K-ATPase in WT and cKO mice at P8. Scale bar: 50 μm.

RNA isolation and real-time PCR
RNA isolation were used TRIzol (Invitrogen, 15596-018) based on the manufacture protocol. The first-strand cDNA was generated by Reverse Transcription System (Promega, A3500). To quantify the mRNA levels using real-time PCR, aliquots of first-stranded cDNA were amplified with gene-specific primers and SYBR Green PCR Master Mix (CWBIOTECH, CW0682A) using a Bio-Rad Real-Time PCR System (CFX96). The PCR reactions contained 10 ng of cDNA, 1× Universal Master Mix, and 200 nM of forward and reverse primers in a final reaction volume of 20 μl. The sequences of primers used for PCRs are listed in Table 1.

Half-life measurement of HuR-targeted transcripts
Ependymal cells were treated with Actinomycin D at a concentration of 10 mM. Cells were collected at four time points after addition (0, 4, 8, and 12 h) by washing once with PBS, then lysing the cells in Buffer RLT from the RNeasy kit (QIAGEN, 74 104) with1% β-Mercaptoethanol. Each sample was normalized for cell number by quantifying DNA content using a Quant-IT PicoGreen dsDNA Assay kit (ThermoFisher, P11496) according to manufacturer instructions. Equal amounts of cellular contents, as measured by DNA quantity, were taken from each sample and 80 pg of luciferase control RNA (Promega, L4561) was added to each sample before RNA purification. Total RNA was then purified using an RNeasy Kit and reverse transcribed using the Reverse Transcription System (Promega, A3500). Real-time PCR was performed on a Step One Plus cycler from Applied Biosystems with Fast SYBR Green Master Mix (CWBIOTECH, CW0682A). Standard curves were generated by plotting CT values against the known initial concentration of luciferase control RNA, and then used to derive mRNA concentration of each target gene at each time point. The ln$^{\text{mRNA}}$ concentrations at

time points 0, 4, 8, and 12 h were then used to perform a linear regression as a function of time and identify the slope of said line as the decay rate (k). Half-life was calculated with the following formula: $t1/2 = \ln^2/kdecay = \ln^2/kdecay$ (Chen et al., 2008).

Western blot analysis
Brains were lysed in ice-cold RIPA buffer (20 mM Tris-HCl, pH 7.5, 100 mM NaCl, 0.1% SDS, and 0.5% sodium deoxycholate) containing Complete Protease Inhibitor Cocktail (Roche, 11697498001). Brain, cell lysates or lysates from RNA-immunoprecipitation assay were resolved on SDS-PAGE and blotted with an antibody against HuR (1:1000, Abcam ab136542), anti-Spef2 (1:500, Bioss, bs-11488R) or anti-Cfap52 (1:500, Abcam, ab170937). Immunoblots were analyzed by Sage capture 2015TM software (SAGECREATION Company, Mini Chemi 610).

Statistical analyses
Data in bar graphs are expressed as mean $\pm$ SEM. The means of two experimental groups were compared with Student's t test using GraphPad Prism 6 software. Differences were considered statistically significant at $p < 0.05$. Vector angles were measured using ImageJ software. The angles of the vectors were normalized so that the average of the angle of the vectors is 180°. The distribution of the angles was compared using Watson's two-sample U^2 test using the Oriana software.

Data and code availability
The data of this manuscript are available from the corresponding authors. All other data are included in the Extended Data or available from the authors upon reasonable requests. The raw RIP-seq and RNA-seq data in this study have been submitted to the Genome Sequence
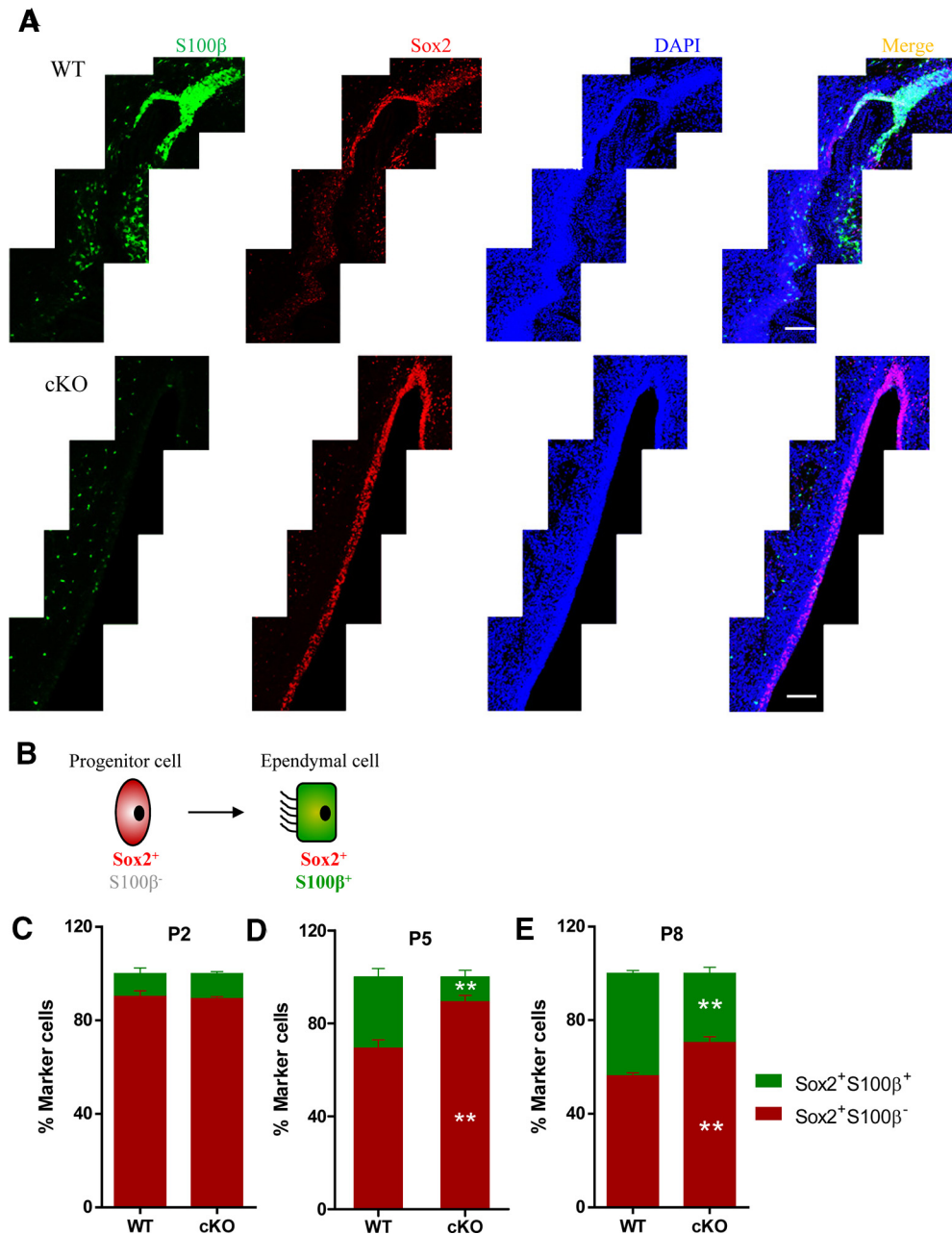
Figure 5. HuR deficiency leads to impaired differentiation of ependymal cells. ***A***, Sample images of brain sections stained with S100β and Sox2 in WT and cKO mice at P8. Scale bar: 100 μm. ***B***, Schematic diagram showing the ependymal cell differentiation with cell lineage markers. ***C–E***, Percentages of Sox2$^-$S100β^+ and Sox2$^+$S100β^- were quantified in WT and cKO mice at P2, P5, and P8. P2, WT = 3 mice; cKO = 3 mice. P5, WT = 5 mice; cKO = 3 mice. P8, WT = 3 mice; cKO = 3 mice. Data are presented as mean ± SEM, *$p < 0.05$, **$p < 0.01$.

Archive in Beijing Institute of Genomics (BIG) Data Center (https://bigd.big.ac.cn/gsa) under accession number CRA003220.

Results

HuR deficiency leads to postnatal hydrocephalus

To investigate the role of HuR in brain development, we generated conditional *HuR* KO mice (cKO) by crossing *HuR^{f/f}* mice with Nestin-Cre transgenic driver mice (Fig. 1*A*). The littermates without *HuR* flox allele were used as WT controls. We confirmed that the expression of HuR was efficiently deleted from the brain of cKO mice (Fig. 1*B*). Although cKO mice appeared grossly normal at birth, they began to exhibit lethargy and growth retardation accompanied by hydrocephalus, which characterized by a swollen, dome-shaped cranium between two and three weeks of age (Fig. 1*C*). The cKO mice then succumbed to death at

approximately three weeks of age (Fig. 1*D*). Histopathological examination revealed that the areas of LV, third and fourth ventricles were comparable between WT and cKO mice at P2 (Fig. 1*E,F*). However, cKO mice exhibited enlarged LV, but normal third and fourth ventricles, at P8 (Fig. 1*G,H*). A severe enlargement of LV was observed in cKO mice at P18 (Fig. 1*I*). Thus, these data suggest that hydrocephalus in HuR-deficient mice is most likely developed postnatally.

Impairments of neural stem cell (NSC) proliferation and neurogenesis in the developing brain is associated with nonobstructive hydrocephalus (Furey et al., 2018). To assess whether HuR deficiency affects NSC proliferation during embryonic brain development, we then performed 2-h BrdU pulse-labeling analysis and found that both WT and cKO mice had comparable numbers of BrdU$^+$Pax6$^+$ apical progenitor cells and BrdU$^+$Tbr2$^+$
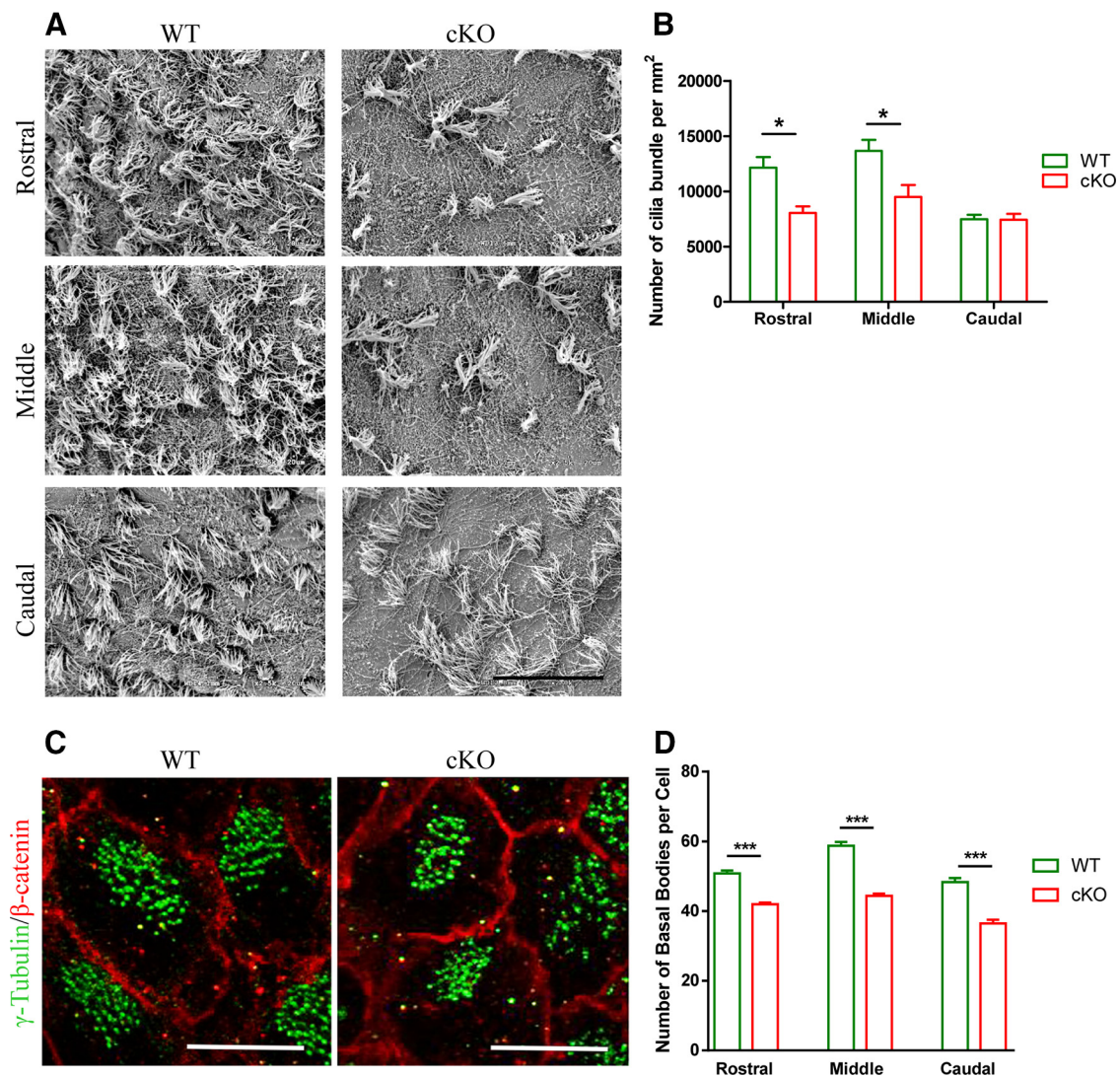
Figure 6. HuR deficiency leads to impaired ciliogenesis of ependymal cells. **A,** Scanning electron micrographs of the LV wall surface in WT and cKO mice from rostral to caudal at P8. Scale bar: 20 μm. **B,** The number of cilia bundles were quantified in WT and cKO mice at P8. WT, $n = 3$ mice; cKO, $n = 3$ mice. Data are presented as mean $\pm$ SEM. **C,** Whole-mount preparations of the LV wall were stained with β-catenin and γ-tubulin in WT and cKO mice. Scale bar: 10 μm. **D,** The numbers of BBs were quantified in WT and cKO mice from rostral to caudal at P8. Rostral: WT, $n = 163$ cells from 3 mice, cKO, $n = 274$ cells from 3 mice. Middle: WT, $n = 164$ cells from 3 mice; cKO, $n = 265$ cells from 3 mice. Caudal: WT, $n = 109$ cells from 3 mice; cKO, $n = 76$ cells from 3 mice. Data are presented as mean $\pm$ SEM; *$p < 0.05$, ***$p < 0.001$.

basal progenitor cells in the ventricular zone/subventricular zone regions of cerebral cortex at embryonic day (E)14.5 (Fig. 2A–C). Next, we investigated the effect of HuR deficiency on NSC differentiation by injecting BrdU at E14.5 and assessing the numbers of BrdU$^+$ cells that also express the postmitotic neuronal marker Tbr1 at E16.5. Moreover, both WT and cKO mice generated similar numbers of BrdU$^+$Tbr1$^+$ neurons in the cerebral cortex (Fig. 2D, E). Furthermore, WT and cKO mice displayed normal distributions of Cux1$^+$, Ctip2$^+$, Satb2$^+$, or Tbr1$^+$ postmitotic projection neurons in the cerebral cortex at P0 (Fig. 2F–I). These findings are consistent with our previous study that HuR deficiency does not affect embryonic neurogenesis (Wang et al., 2019). Therefore, hydrocephalus in HuR-deficient mice is unlikely caused by impairments of NSC proliferation and neurogenesis during embryonic brain development.

Sylvian aqueductal stenosis is frequently associated with congenital hydrocephalus (Casey et al., 1997; Huh et al., 2009). However, the sylvian aqueduct of cKO mice was expanded normally compared with WT mice (Fig. 3A,B), suggesting hydrocephalus in cKO mice was not cause by occlusion in the sylvian

aqueduct. Furthermore, the subcommissural organ (SCO) is a secretory gland located immediately anterior to the sylvian aqueduct underneath the posterior commissure, which is able to secrets glycoproteins to facilitate CFS flow and defective SCO is associated with hydrocephalus (Huh et al., 2009). Whereas, the size of SCO was comparable between WT and cKO mice (Fig. 3C). In addition, abnormality of choroid plexus that produces CSF can also result in hydrocephalus (Miyan et al., 2003). Nevertheless, the size of choroid plexus was comparable between WT and cKO mice (Fig. 3D,E). The expression of the homeobox transcription factor Otx2 (Fig. 4A,B) and the localization of Na/K ATPase and E-cadherin of general polarity (Fig. 4C) in choroid plexus were not significantly affected in cKO mice, suggesting that choroid plexus develops normally in HuR-deficient mice.

HuR deficiency impairs ependymal cell differentiation and apical docking of BBs

Multiciliated ependymal cells lining the ventricular wall promote the direction of CSF flow (Del Bigio, 2010; Ohata and Alvarez-

Buylla, 2016). Ependymal cells are derived from NSCs and become mature in the first postnatal week (Spassky et al., 2005). Alterations in differentiation and ciliogenesis of ependymal cells result in hydrocephalus (Jacquet et al., 2009; Mirzadeh et al., 2010b; Tissir and Goffinet, 2013). Since hydrocephalus in cKO mice was observed at the end of the first post-natal week, we therefore investigated whether HuR deficiency leads to defective development of ependymal cells (Fig. 5A,B). We found that there were similar numbers of Sox2$^+$S100β^- NSCs and Sox2$^+$S100β^+ ependymal cells in WT and cKO mice at P2 (Fig. 5C). However, starting from P5, cKO mice persisted higher numbers of Sox2$^+$S100β^- NSCs, but fewer numbers of Sox2$^+$S100β^+ ependymal cells, compared with WT mice (Fig. 5D). At P8, cKO mice constantly generated significant fewer numbers of Sox2$^+$S100β^+ ependymal cells (Fig. 5E). These data suggest that HuR is required for ependymal cell differentiation.

By using scanning electron microscopy, we observed that there were in general fewer cilia tufts in cKO mice than in WT mice at P8 (Fig. 6A). Quantification analysis revealed that cKO mice exhibited fewer numbers of cilia bundle in the rostral and middle, but not caudal, LV wall (Fig. 6B). Cilia are nucleated from microtubule-based BBs (Marshall, 2008). By using an antibody against γ-tubulin to label the ciliary BB and N-cadherin to high-light cell boundary, we found that the numbers of BB in individual ependymal cell were significantly fewer in the rostral, middle and caudal LV wall of cKO mice at P8, compared with WT mice (Fig. 6C,D). In multiciliated cells, BBs are formed *de novo* in the cytoplasm, and transported apically to the plasma membrane, where docking occurs (Dawe et al., 2007). By performing transmission electron microscopy analysis, we found that the BBs showed typical 9 + 0 ring of microtubule triplets in both WT and cKO ependymal cells (Fig. 7B), suggesting HuR deficiency does not significantly affect the architecture of BB. However, some BBs were stagnated in the cytoplasm and failed to localize apically and dock at the apical membrane in HuR-deficient ependymal cells (Fig. 7A). Hence, these data suggest that HuR is involved in governing apical docking of BBs in ependymal cells.

HuR deficiency disrupts ependymal flow and ciliary coordination of ependymal cells

The coordinated beating of cilia on the apical surface of ependymal cells generates directional CSF flow, which is known as ependymal flow (Miyan et al., 2003). Defects in ependymal flow can cause hydrocephalus (Ibanez-Tallon et al., 2003; Matsuo et al., 2013). To evaluate the dynamics of ependymal flow, we placed polystyrene latex fluorescent microbeads on the live preparations of the LV walls and monitored the migration of beads across their surface (Fig. 8A). The velocity can be quantified by measuring the distance that fluorescent microbeads travel within a defined time (Movies 1, 2; Fig. 8B). On the LV wall of WT mice, the movements of the fluorescent

WT   cKO

A Docking   BB BB BB   BB BB BB

B Basal Body   9+0   9+0

C Axoneme   9+2   9+2
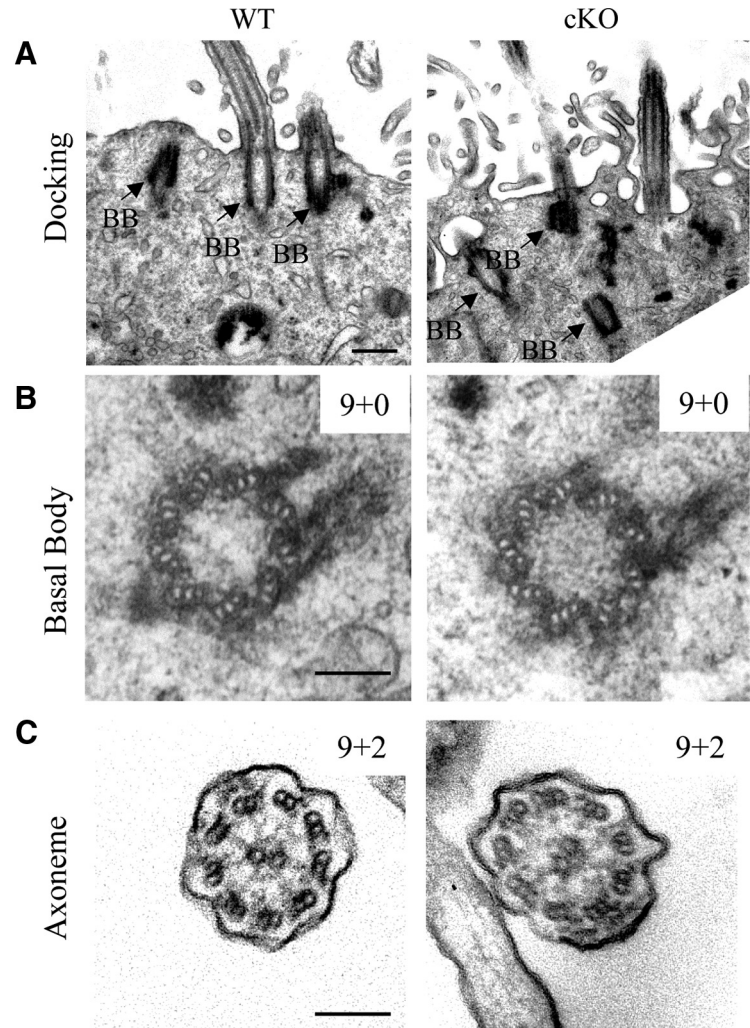
Figure 7. Ciliary axonemal microtubule organization in WT and cKO mice. *A*, TEM transverse sections on cilia of ependymal cell shows that some BBs fail to dock at the apical membrane and remain in the cytoplasm in cKO mice at P8. Scale bar: 200 nm. *B*, TEM transverse sections through the BB showed a normal structure of 9 + 0 triplet microtubules in cKO mice at P8. Scale bar: 100 nm. *C*, Axonemal transverse sections revealed a normal structure of 9 + 2 doublet microtubules in cKO mice at P8. Scale bar: 100 nm.

microbeads were detected by a strong dorsal-to-ventral current (Fig. 8B; Movie 1). However, the movements of microbeads on the LV wall of cKO mice exhibited slower overall speed (Fig. 8B,C; Movie 2) and lower directionality (Fig. 8D,E; Movie 2) than the bead movements on the LV wall of WT mice. These results suggest that HuR deficiency leads to impaired CSF normal circulation.

The core, also known as the axoneme, of motile cilia on the ependymal cell has a 9 + 2 microtubule structure with nine doublet microtubules surrounding a central microtubule pair (Ibanez-Tallon et al., 2003; Satir and Christensen, 2007). The structure integrity of axoneme is required for generation of ciliary motor force (Satir and Christensen, 2007). We then performed transmission electron microscopy analysis to examine the potential substructure differences of motile cilia between WT and cKO mice. However, we found that the ultrastructure of ependymal cilia in cKO mice retained a normal 9 + 2 structure of motile cilia (Fig. 7C), suggesting that HuR deficiency may not affect the inner cilia structure.

The glycosyl phosphatidylinositol-anchored sialoglycoprotein CD24 localizes to the motile cilia of ependymal cells (Guirao et
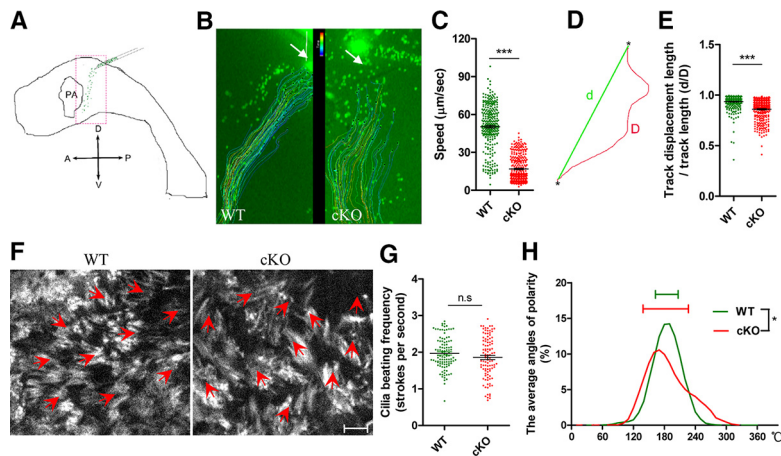
Figure 8. HuR deficiency leads to disruption of ependymal flow. **A,** Schematic of the ependymal flow assay. Fluorescent beads (green) were filled in a glass needle and placed on to whole-mount preparations of the lateral walls of LV. A, anterior; D, dorsal; P, posterior; V, ventral. **B,** Migratory patterns of the fluorescent beads on LV walls of WT and cKO mice were recorded. See also Movies 1, 2. Arrows indicate where fluorescent beads were filled. Colored lines indicate the trajectories of individual beads. Scale bar: 100 μm. **C,** Overall speed of the beads' migration was quantified in WT and cKO mice. Data are present as means ± SEM. Each point on the graph is the speed of an individual fluorescent beads. **D,** Directionality (d/D) was represented as the distance (d) between first point and final point divided by the bead pathway (D). **E,** Overall directionality was quantified in WT and cKO mice. Data are present as means ± SEM. Each point on the graph is the speed of an individual fluorescent beads. **F,** The representative images of the ciliary beating in WT and cKO mice. See also Movie 3, 4. The arrows indicate the direction of ciliary beating. Scale bar: 20 μm. **G,** CBF was quantified in WT and cKO mice. Data are presented as means ± SEM. Each point on the graph is the CBF of an individual ependymal cell. **H,** Histogram showing the distribution of cilia beating direction in WT and cKO mice. Error bars on the graph show CSD; $*p < 0.05$, $***p < 0.001$.

al., 2010). We labeled whole-mount preparation of the lateral ventral walls with anti-CD24 antibody conjugated with phycoerythrin (PE) to monitored cilia behavior (Fig. 8F; Movies 3, 4). The ciliary beating frequency (CBF; strokes per second) in WT and cKO mice was not significantly different (Fig. 8G), suggesting the reduction in the speed of ependymal flow in cKO mice was not because of defects in CBF. However, the deviation of the cilia movement direction, which is expressed as the circular SD (CSD; drawn as an error bar on the graph) from the main direction of cilia bundle for each ependymal cell, was significantly larger in cKO mice than in WT controls (Fig. 8H), suggesting that HuR deficiency impairs cilia coordination in ependymal cells.

HuR deficiency disturbs translational and rotational polarity of ependymal cells

Coordinated ciliary beating and parallel ciliary bundles are derived from the translational and rotational polarity of planar polarized BBs in ependymal cells (Spassky and Meunier, 2017). Moreover, ependymal PCP is initiated and organized by cilia (Mirzadeh et al., 2010b). Given the defective ciliogenesis has been found in HuR-deficient ependymal cells, we then hypothesized that the ependymal PCP would be affected. To evaluate the translational polarity, we stained a whole mount of the LV walls with antibodies against γ-tubulin, which labels BBs, and β-catenin, which labels intercellular junctions. The planar positions of BB clusters were measured as the angle from the center of the apical surface of a single cell to the center of BB cluster. The BB clusters of WT mice were deflected to the same side of each cell in the LV wall (Fig. 9A,B). However, BBs in LV wall of cKO mice were consistently clustered on any particular side within each cell (Fig. 9A,B). Quantitative analysis revealed that the angle of BB clusters had a significantly wider distribution in the LV wall of cKO mice compared with WT mice (Fig. 9C). Moreover, the BB displacement distance, which represents remoteness from the center of the apical cell surface (Fig. 9D), was significantly shorter in ependymal cells at the rostral, middle and caudal ventricular walls of cKO mice than WT mice (Fig. 9E–G). On the other hand, translational polarity is first established in RGCs, then the BB angle is further refined during postnatal development (Spassky et al., 2005; Mirzadeh et al., 2010b). To address whether HuR functions in the establishment of translational polarity before ependymal cell differentiation, we investigated the BB angle in WT and cKO mice at P2 (Fig. 9H,I). BBs also had a wider distribution in the LV wall of cKO mice compared with WT mice (Fig. 9J), indicating that HuR deficiency affects translational polarity of the primary cilia in RGCs. Moreover, the BB displacement distance was significantly shorter in RGCs of cKO mice than in WT mice (Fig. 9K). Thus, these results suggest that HuR deficiency disrupts the translational polarity of ependymal cells within the LV wall.

Each BB has rotational polarity based on its orientation with respect to its basal foot (BF; Wallingford, 2010). CEP164 is
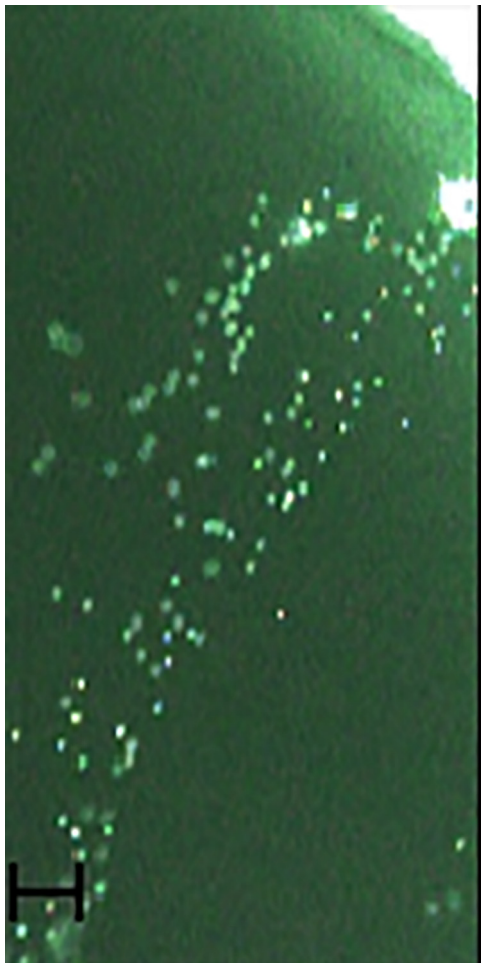
Movie 1. Live imaging movie showing the migration of fluorescent beads on the whole mount preparation of the lateral wall of the lateral ventricle in WT mouse. [View online]
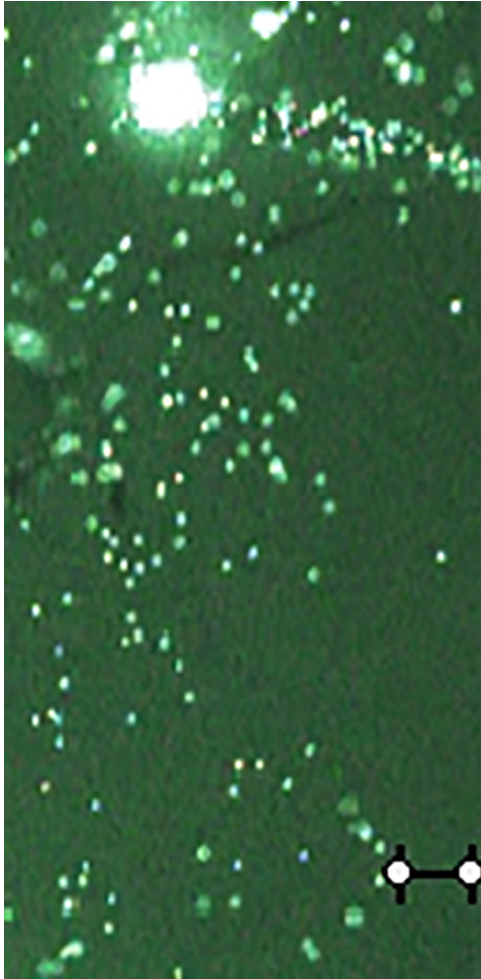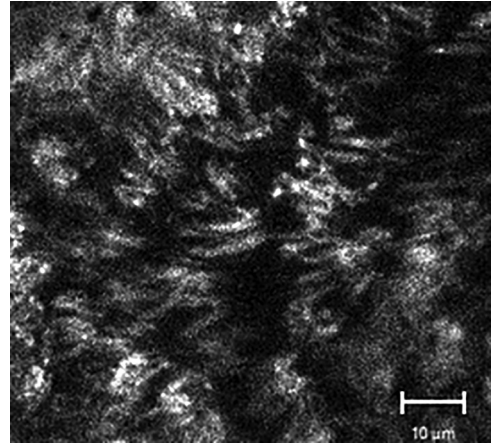
Movie 2. Live imaging movie showing the migration of fluorescent beads on the whole mount preparation of the lateral wall of the lateral ventricle in cKO Mouse. [View online]
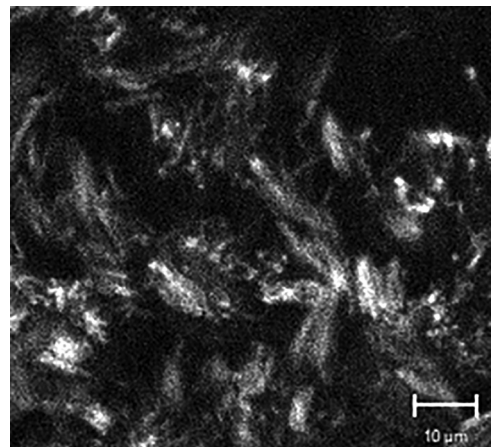

Movie 3. Live imaging movie showing ciliary beating of ependymal cells in WT mouse. [View online]

Movie 4. Live imaging movie showing ciliary beating of ependymal cells in cKO mouse. [View online]

asymmetrically localized to the distal appendages in one side of the BB, while γ-tubulin localized to the BB (Fig. 10A). We then drew a vector from the CEP164$^+$ distal appendage to the γ-tubulin$^+$ BB to quantify the rotational polarity of individual BB. The rotational angle of BF in each ependymal cell had a significantly wider distribution in cKO mice than in WT mice (Fig. 10B). By calculating the dispersion of BF directions within single ependymal cell ($r = 1$ – circular variance), we found that the r value within single ependymal cell was significantly smaller in cKO mice than in WT mice (Fig. 10C). Moreover, the BF protrudes laterally from the BB and points in the direction of CSF flow (Mirzadeh et al., 2010b). We then employed transmission electron microscopy analysis to further analyze the rotational polarity in cKO mice (Fig. 10D). In contrast to WT mice, cKO mice exhibited a significantly wider distribution of the BF rotational angle (Fig. 10E) and a significant smaller r value of BF dispersion within single ependymal cell (Fig. 10E). Therefore, these data suggest that HuR deficiency impairs the coalignment in rotational polarity of BB in individual ependymal cell.

HuR stabilizes its targeted transcripts related to ependymal cell function

To determine the mechanistic function of HuR in ependymal cells, we performed RNA-immunoprecipitation followed by high-throughput sequencing (RIP-seq) in primary culture ependymal cells from neonatal mouse brain. Consistent with *in vivo* observation, there were significant fewer differentiated cells with multicilia from cKO mice than those from WT controls *in vitro* (Fig. 11A,B). By analyzing the RIP-seq data, we then identified 662 HuR-bound gene transcripts in ependymal cells (Fig. 11C,D; Extended Data Fig. 11-1). Our analysis showed the enriched distribution of HuR-binding sites on the 3′ untranslated region (UTR; Fig. 11E,F), suggesting that HuR regulates the stability of its target mRNAs in ependymal cells. GO analyses of HuR-targeted transcripts revealed enrichment of genes related to cell differentiation, cilia formation and epithelial cell polarity (Fig. 11G). Next, we performed RNA-seq analysis on primary culture ependymal cells from WT and cKO neonatal mice (Fig. 12A,B). We then identified 1720 gene transcripts that were significantly differentially expressed between WT and cKO ependymal cells [fold change > 0.2; false discovery rate (FDR) q < 0.005]. Of these, 875 were expressed at significantly higher levels, and 845 were expressed at significantly lower levels in HuR-deficient cells (Extended Data Fig. 12-1). GO analyses revealed upregulated genes related to Fc-γ receptor signaling and synapse pruning (Fig. 12C), while downregulated genes related to cilium organization, cilium assembly and microtubule bundle formation (Fig. 12D). To
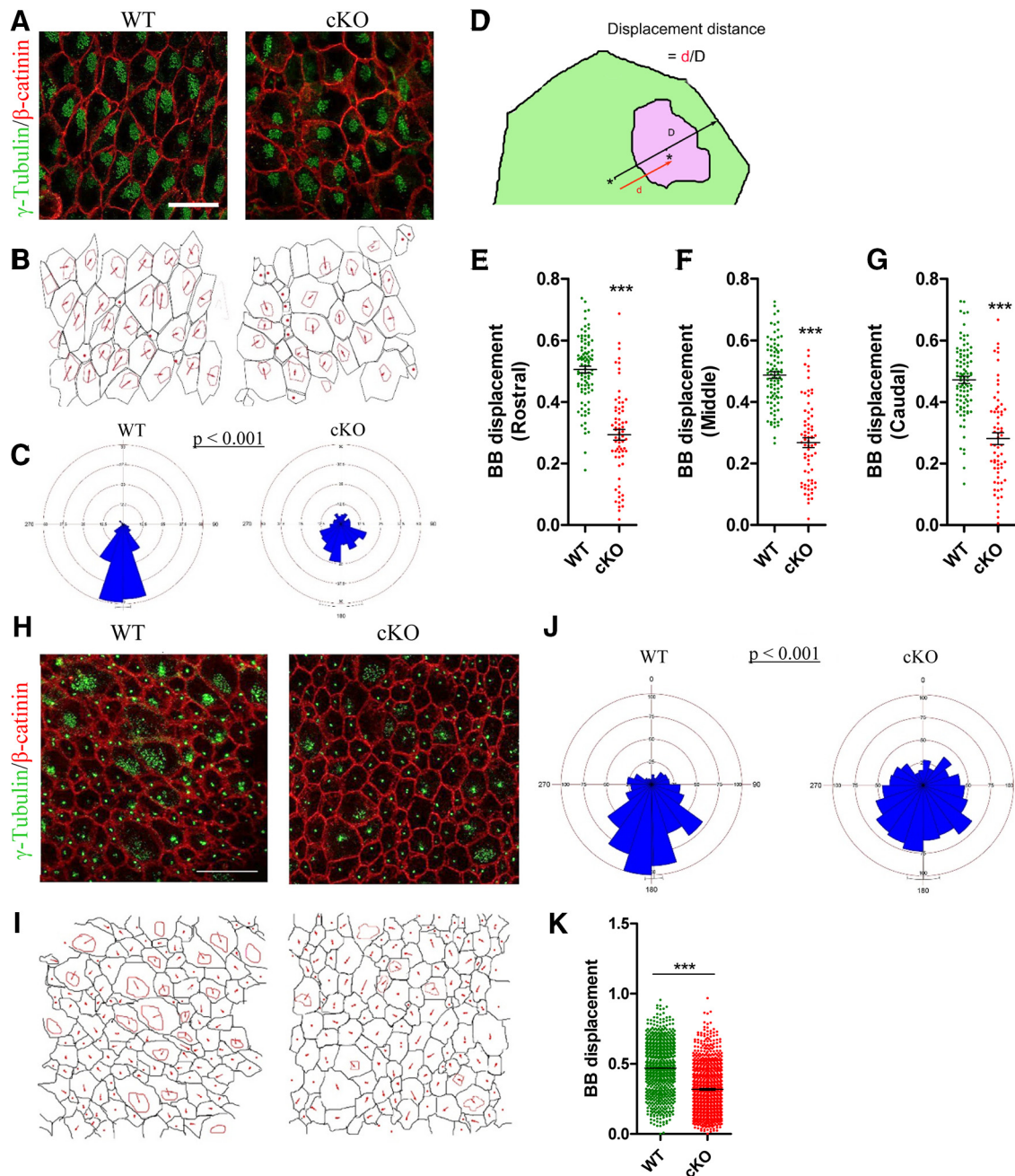
Figure 9. HuR deficiency leads to impaired translational polarity of ependymal cells. ***A***, Whole-mount preparations of LV walls from WT and cKO mice at P8 were stained with antibodies against γ-tubulin and β-catenin. Scale bars: 20 μm. ***B***, The traces of the intercellular junction labeled with β-catenin and BB labeled with γ-tubulin of ependymal cells. The red arrows show the vectors drawn from the center of the apical surface to that of the BB patch in ependymal cells. ***C***, The distribution of BB patch angles in WT and cKO mice were plotted on a circular diagram. ***D***, Schematic drawing showing the displacement distance of a BB cluster. The distance (d, red arrow) between the centroid of the cell and the centroid of the BB cluster were normalized to the distance (D, black arrow) of the line extended to the cell edge. ***E–G***, Displacement distance of a BB cluster was quantified at rostral (***E***), middle (***F***), and caudal (***G***) regions in WT and cKO mice. Each point on the graph is the displacement distance of an individual BB cluster. ***H***, The whole-mount preparations of the LV walls at P2 were stained with antibodies against γ-tubulin and β-catenin in WT and cKO mice. Scale bars: 20 μm. ***I***, The traces of the intercellular junction labeled with β-catenin and BB labeled with γ-tubulin of radial glial cells. The red arrows show the vectors drawn from the center of the apical surface to that of the BB patch in radial glial cells. ***J***, The distribution of the BB patch angles were plotted on a circular diagram at P2 ($p < 0.001$). WT, $n = 725$ cell; cKO, $n = 880$ cell. ***K***, Displacement distance of a BB cluster was quantified in WT and cKO mice. Each point on the graph is the BB displacement distance of an individual radial glial cell ($p < 0.001$). WT, $n = 724$ cell; cKO, $n = 878$ cell. Data are presented as means ± SEM; ∗∗∗$p < 0.001$.

determine the functional consequence of HuR on its target transcripts, we integrated and combined the RNA-seq data from HuR-deficient ependymal cells with the RIP-seq data. We found a total of 121 HuR-bound transcripts that were affected by loss of HuR with a more than 0.2-fold difference (Fig. 12E; Extended Data Fig. 12-2). Given the distribution

of HuR-binding sites were enriched on the 3′UTR (Fig. 11E, F), we then treated primary cultured ependymal cells from WT and cKO neonatal mice with actinomycin D to halt *de novo* transcription and performed RNA-seq at 0 and 5 h later to obtain the ratio of mRNA levels for each gene to measure their stability. Across the transcriptomes, HuR-
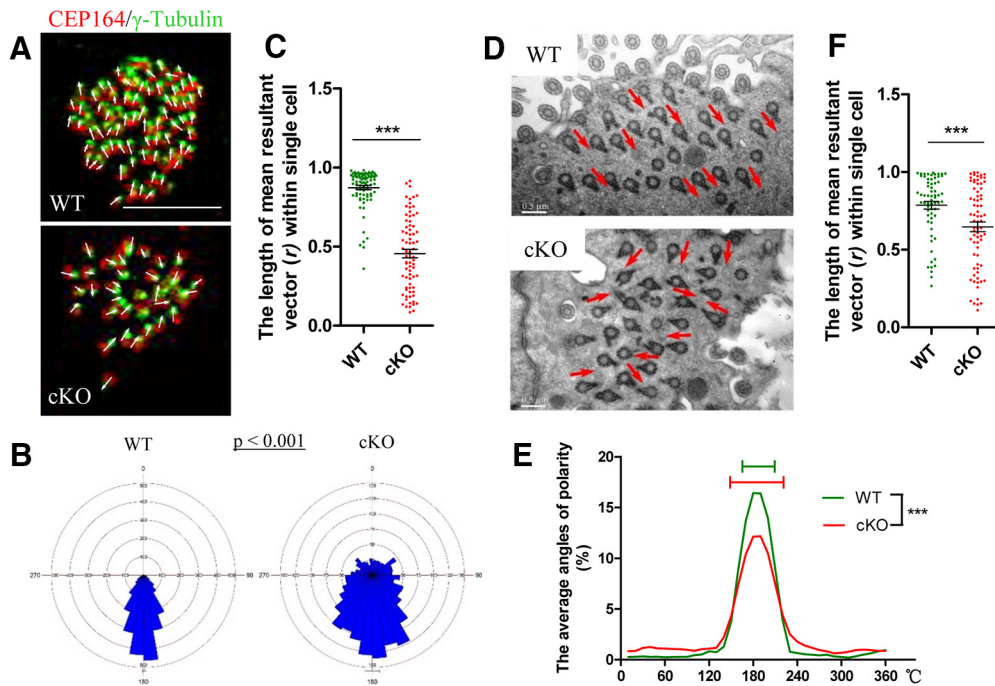
Figure 10. HuR deficiency leads to impaired rotational polarity of ependymal cells. ***A***, Whole-mount preparations of LV walls from WT and cKO mice at P8 were stained with antibodies against γ-tubulin and CEP164. Scale bars: 20 μm. ***B***, The distribution of the BF patch angles in WT and cKO mice were plotted on a circular diagram. ***C***, The dispersion of BF directions (from CEP164 to γ-tubulin) within single ependymal cell of WT and cKO mice was measured as r ($r = 1$ – circular variance). Data are presented as means $\pm$ SEM. ***D***, TEM analysis showing the orientations of individual BB (arrows) in WT and cKO mice. Scale bar: 500 nm. ***E***, Histogram showing the distribution of the BB angles in WT and cKO mice. Error bars on the graph show CSD. ***F***, The distribution of BF patch angles within single ependymal cell was measured as r from TEM analysis. Data are presented as means $\pm$ SEM; ***$p < 0.001$.
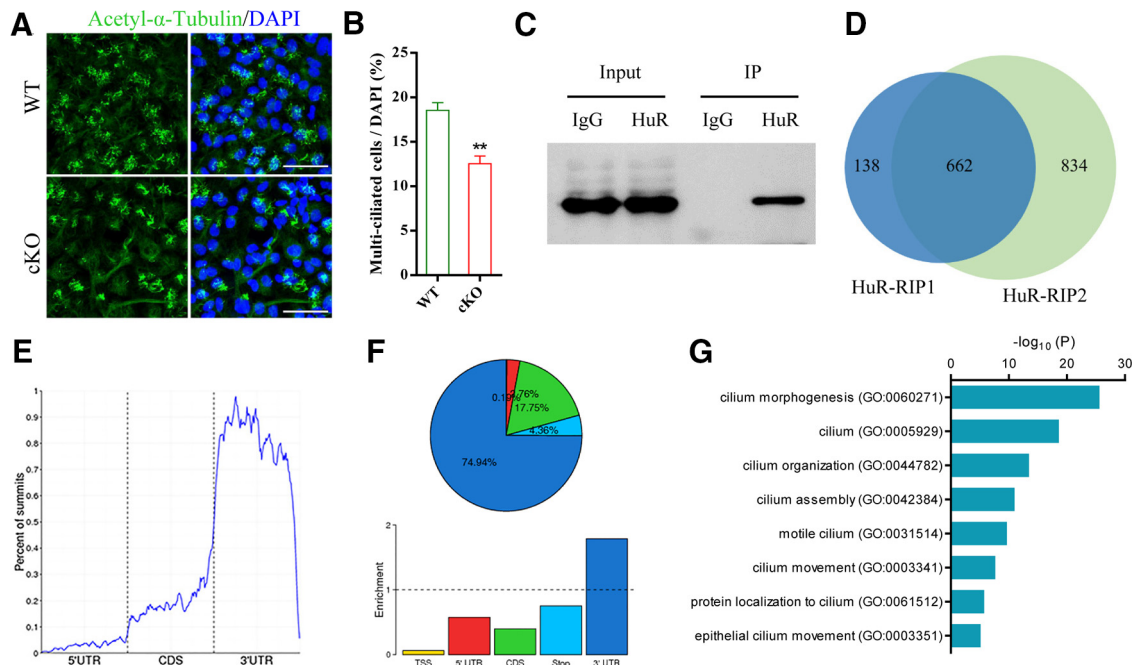
Figure 11. High-throughput analysis of HuR-targeted mRNA transcripts in ependymal cells. ***A***, Sample images of *in vitro* cultured WT and cKO ependymal cells staining with antibody against acetyl-α-tubulin. Scale bars: 50 μm. ***B***, Quantification of cultured multiciliated cells from WT and cKO mice ($p = 0.008$). WT, $n = 6$ independent experiments; cKO, $n = 6$ independent experiments. ***C***, Western blot analysis of HuR RNA-RIP from ependymal cells. ***D***, Venn diagram showing intersection among HuR-targeted genes identified in two independent RIP-seq experiments (Extended Data Fig. 11-1). ***E***, Histogram showing HuR RIP-seq reads along a normalized mRNA transcript. ***F***, Enrichment of HuR RIP peak in five nonoverlapping transcript segments. Pie chart shows percentage of peaks annotated to each segment. Bar plot shows fold enrichment of peaks for each segment, normalized for the segment length. ***G***, Diagram of GO (biological process) terms that are significantly enriched in HuR-targeted genes. Data represent as mean $\pm$ SEM; *$p < 0.05$.
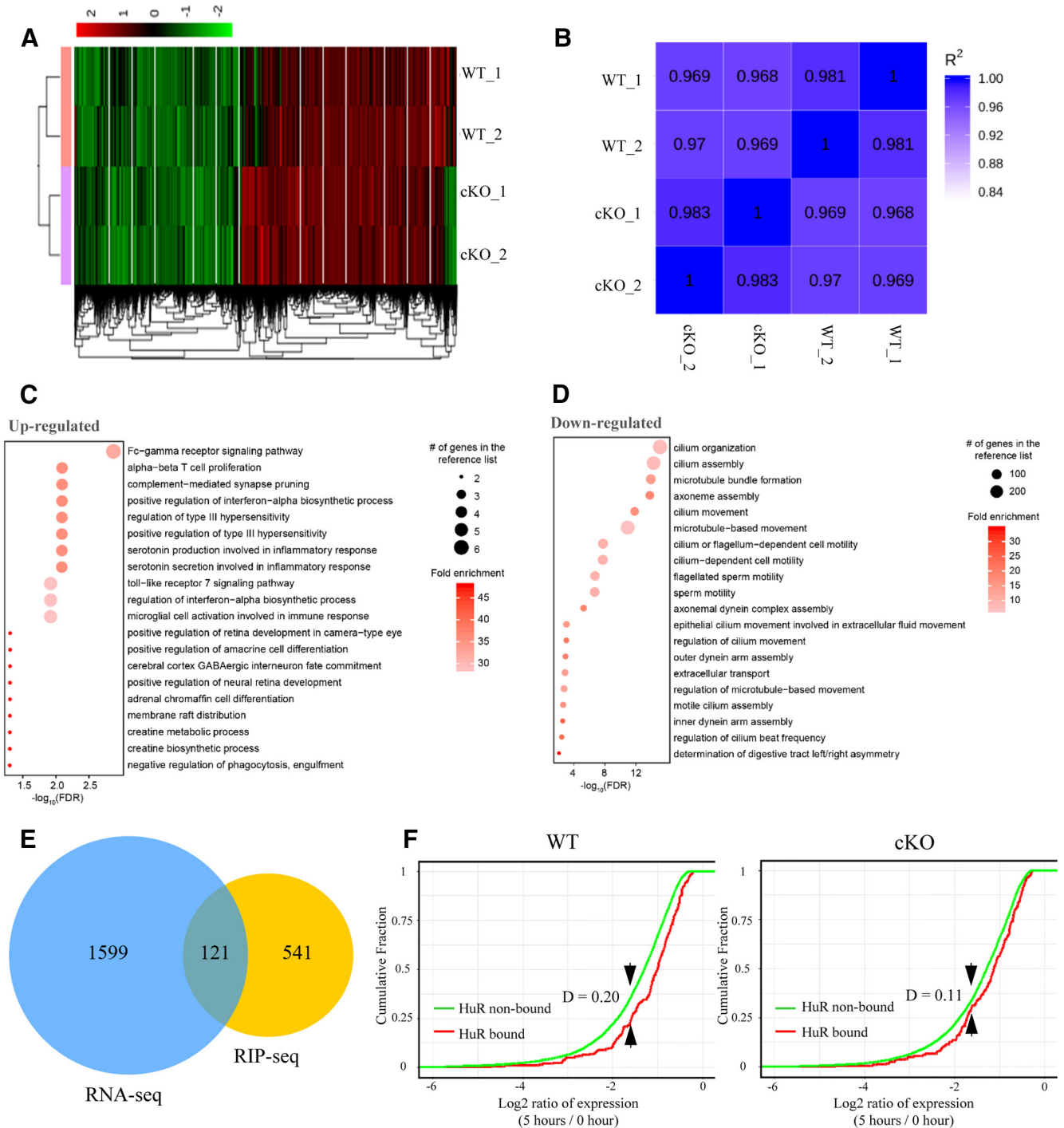
Figure 12. HuR regulates the stability of its targeted transcripts related to ependymal cell development and ciliogenesis. **A**, A heat-map of expression levels (log$_2$RPKM; reads per kb of exon per million mapped reads) of deferential expression genes in WT and cKO ependymal cells and their replicates (Extended Data Fig. 12-1). **B**, An expression heatmap of sample-to-sample distances on the matrix using the whole gene expression profiles among WT and cKO ependymal cells and their replicates. **C**, **D**, Diagram of GO (biological process) terms that are significantly enriched in DEGs. Categories in **C** are enriched in upregulated genes in cKO ependymal cells. Categories in **D** are enriched in downregulated genes in cKO ependymal cells. **E**, Venn-diagram showing the relationship between genes with differential mRNA expression (mRNAs) and mRNA bound by HuR (targets; Extended Data Fig. 12-2). **F**, Cumulative distribution of log2(gene expression ratios) at time 5 h after actinomycin D treatment over time 0 h for HuR-bound genes (red line) and non-HuR-bound genes (green line) for WT and cKO ependymal cells. D represents the value of Kolmogorov–Smirnov test statistic corresponding to the maximum difference between HuR-bound and non-HuR-bound distributions (Extended Data Fig. 12-3).

bound transcripts were exhibited significantly higher ratios than HuR-unbound transcripts in the WT ependymal cells (Fig. 12F; Extended Data Fig. 12-3), and this difference was reduced in HuR-deficient ependymal cells (Fig. 12F; Extended Data Fig. 12-3), suggesting that HuR primarily acts as a stabilizing RBP in ependymal cells.

HuR regulates development of ependymal cells by stabilizing *Cfap52* mRNA

To understand the causal relationship between the molecular function of HuR in ependymal cells and hydrocephalus, we integrated and combined hydrocephalus data set (Rouillard et al., 2016) with our RNA-seq and RIP-seq data (Fig. 13A). From
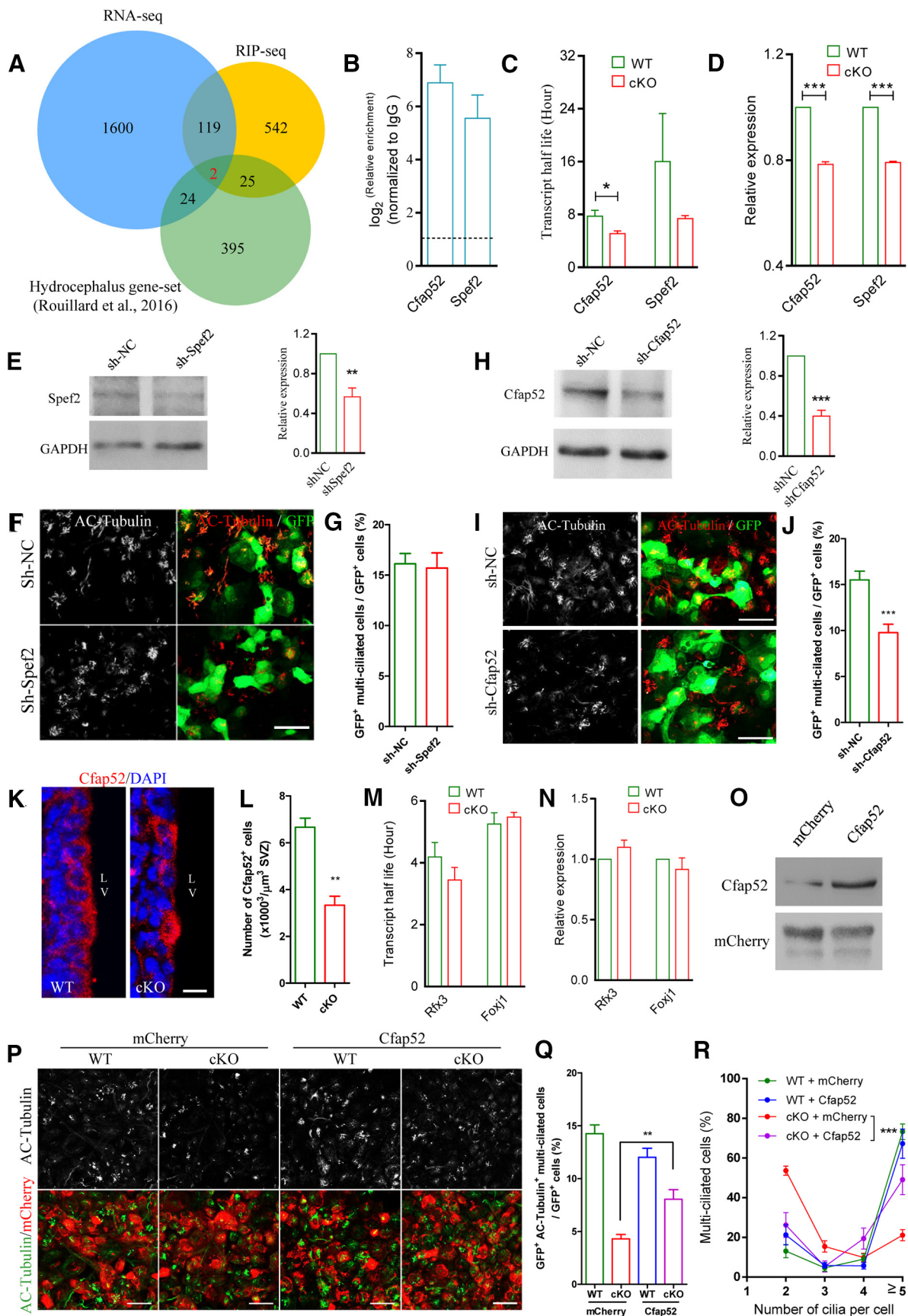
Figure 13. HuR governs ciliogenesis by stabilizing Cfap52 mRNA in ependymal cells. **A**, Venn-diagram showing the relationship between genes with differential mRNA expression (mRNAs), mRNA bound by HuR (targets) and hydrocephalus gene set. **B**, RT-qPCR analysis of *Cfap52* and *Spef2* mRNAs immunoprecipitating with HuR in ependymal cells. HuR-IP, $n = 3$ independent

these comparisons, we identified two gene transcripts, cilia and flagella associated protein 52 (*Cfap52*) and sperm flagellar 2 (*Spef2*), which were highly associated with HuR (Fig. 13*B*), and mutation of these two individual gene cause hydrocephalus (Hirschner et al., 2007; Sironen et al., 2011). HuR deficiency led to shorten the half-life of these two mRNAs in ependymal cells (Fig. 13*C*). Furthermore, we confirmed that their mRNA expression levels were significantly decreased in cKO ependymal cells compared with WT control (Fig. 13*D*). To further investigate the functional role of these two HuR-targeted genes in ependymal cells, we generated shRNAs to knock-down *Cfap52* and *Spef2*, respectively (Fig. 13*E,G*). Knock-down of *Cfap52*, but not *Spef2*, led to fewer differentiated cells with multicilia than the control shRNA *in vitro* (Fig. 13*E–J*), which phenocopied the defective development of ependymal cells in cKO mice. By performing immunofluorescence analysis for Cfap52 in brain sections with LV wall, we found that the numbers of Cfap52$^+$ ependymal cells were significant fewer in cKO mice compared with WT mice (Fig. 13*K,L*), suggesting that HuR is required for Cfap52 expression. Cfap52, also known as Wdr16, is specifically expressed in ciliary tissues, including ependymal cells (Hirschner et al., 2007). Cfap52 has been identified as the effector gene of Foxj-1 and Rfx factors, which is the key transcriptional regulators required for the differentiation of motile ciliated cells and ciliogenesis (Lemeille et al., 2020; Newton et al., 2012). However, HuR deficiency did not affect the half-life and the expression of Foxj-1 and

regulatory factor X-3 (Rfx-3) mRNAs (Fig. 13*M,N*), suggesting that downregulation of *Cfap52 mRNA* expression was unlikely because of altered transcriptional regulation by Foxj-1 and Rfx-3 in HuR-deficient ependymal cells. To this end, we investigated whether re-expression of Cfap52 into HuR-deficient ependymal cells could rescue the defective development of ependymal cells. Although overexpression of Cfap52 did not significantly increase the numbers of differentiated cells with multicilia from WT mice (Fig. 13*O–R*), it was able to increase the numbers of differentiated cells with multicillia from cKO mice (Fig. 13*O–R*). All together, these results suggest that HuR governs ependymal cell development by stabilizing *Cfap52* mRNA; loss of HuR expedites the decay of *Cfap52* mRNAs, resulting in defective ependymal cells and hydrocephalus.

Discussion

In this study, we found that HuR is dispensable for embryonic NSCs proliferation and neurogenesis, but ependymal cell development and ciliogenesis are highly dependent on HuR during postnatal brain development. Brain specific deletion of HuR leads to impaired ependymal cell differentiation, defective ciliogenesis and disorganized ciliary planar polarity, thereby resulting in postnatal congenital hydrocephalus. Mechanistically, HuR binds to *Cfap52* mRNA, which is essential for ciliogenesis. HuR deficiency leads to decreased expression levels of *Cfap52* mRNA because of attenuating its stability (Fig. 14). Therefore, our results unravel the important role of HuR in posttranscriptional regulation of ependymal cell development.

In comparison to current study by using Nestin-Cre mice, deletion of HuR by using Emx1-Cre mice leads to a mild hydrocephalus (data not shown) in our previous study (Wang et al., 2019). Because Emx1-Cre recombinase is expressed exclusively in the dorsal telencephalon of embryonic brain, while Nestin-Cre recombinase is expressed in the entire central nervous system during brain development. However, deletion of HuR in adult brain using Nestin-CreERT2 mice after tamoxifen injection, the mice do not display obvious hydrocephalus phenotype (Wang et al., 2019). These data suggest that HuR is required for ependymal cell development, but not for their maintenance. During brain development, HuR is primarily, if not entirely, expressed in the cytoplasm before P7 but switched from predominantly cytoplasmic to predominantly nuclear localization at P21 and beyond (Wang et al., 2019). By staining HuR with ependymal cell marker S100β in brain sections, we found that HuR is mainly expressed in cytoplasm of ependymal cells at P2, then begin to translocate into nucleus at P7, eventually is localized in the nucleus at P14 (data not shown). However, the hydrocephalus phenotypes in cKO mice were appeared before the translocation of HuR from cytoplasm to nucleus, suggesting that cytoplasmic HuR is required for the development of ependymal cells. The HuR RIP-seq analysis showed the enriched distribution of HuR-binding sites on the 3′UTR, suggesting that HuR regulates the stability of target mRNAs in ependymal cells. Furthermore, we demonstrated that HuR regulates development of ependymal cells by stabilizing Cfap52 mRNA. In contrast to the cytoplasmic function of HuR in ependymal cell development, nuclear localization of HuR is essential for adult NSC proliferation and neurogenesis (Wang et al., 2019). Transcriptomic analysis of HuR-deficient adult NSCs reveals that HuR primarily

←

experiments; IgG-IP, $n = 3$ independent experiments. **C**, The half-life of *Cfap52* and *Spef2* mRNA transcripts in WT and cKO ependymal cells. WT, $n = 3$ independent experiments; cKO, $n = 3$ independent experiments. **D**, The relative expression of *Cfap52* and *Spef2* mRNAs in WT and cKO ependymal cells. WT, $n = 3$ independent experiments; cKO, $n = 3$ independent experiments. **E**, Western blot analysis (left) and quantification (right, $p = 0.008$) of the efficacy of shRNA against Spef2. sh-NC, $n = 3$ independent experiments; sh-Spef2, $n = 3$ independent experiments. **F**, Sample images of *in vitro* lenti-sh-NC and lenti-sh-Spef2 infected ependymal cells staining with antibody against acetyl-α-tubulin. Scale bars: 50 μm. **G**, Quantification of lenti-sh-NC and lenti-sh-Spef2 infected multiciliated cells ($p = 0.811$). sh-NC, $n = 3$ independent experiments; sh-Spef2, $n = 3$ independent experiments. **H**, Western blot analysis (left) and quantification (right, $p < 0.001$) of Cfap52 expression in lenti-sh-NC and lenti-sh-Cfap52 infected cells. sh-NC, $n = 3$ independent experiments; sh-Cfap52, $n = 3$ independent experiments. **I**, Sample images of *in vitro* lenti-sh-NC and lenti-sh-Cfap52 infected ependymal cells staining with antibody against acetyl-α-tubulin. Scale bars: 50 μm. **J**, Quantification of lenti-sh-NC and lenti-sh-Cfap52 infected multiciliated cells ($p = 0.0003$). sh-NC, $n = 3$ independent experiments; sh-Cfap52, $n = 3$ independent experiments. **K**, Sample images of brain sections stained with Cfap52 in WT and cKO mice at P8. Scale bar: 20 μm. **L**, Quantification of Cfap52 positive cells in the LV of WT and cKO mice ($p = 0.0036$). WT, $n = 3$ mice; cKO, $n = 3$ mice. **M**, The half-life of Foxj-1 and Rfx-3 mRNA transcripts in WT and cKO ependymal cells. WT, $n = 3$ independent experiments; cKO, $n = 3$ independent experiments. **N**, The relative expression of Foxj-1 and Rfx-3 mRNAs in WT and cKO ependymal cells. WT, $n = 3$ independent experiments; cKO, $n = 3$ independent experiments. **O**, Western blot analysis of Cfap52 expression in lenti-mcherry and lenti-Cfap52-mCherry infected cells. **P**, Sample images of WT and cKO ependymal cells *in vitro* infected with lenti-mCherry or lenti-mCherry-Cfap52 and stained with antibody against acetyl-α-tubulin. Scale bars: 50 μm. **Q**, Quantification of WT and cKO ependymal cells infected with lenti-mCherry or lenti-mCherry-Cfap52. WT + lenti-mCherry versus WT + lenti-mCherry-Cfap52, $p = 0.0972$, cKO + lenti-mCherry versus cKO + lenti-mCherry-Cfap52, $p = 0.002$. **R**, Distribution of multiciliated cells from WT and cKO mice infected with lenti-mCherry or lenti-mCherry-Cfap52. WT + lenti-mCherry, $n = 3$ independent experiments; WT + lenti-mCherry-Cfap52, $n = 3$ independent experiments. cKO + lenti-mCherry, $n = 3$ independent experiments; cKO + lenti-mCherry-Cfap52, $n = 3$ independent experiments. Data represent as mean ± SEM; $*p < 0.05$, $**p < 0.01$, $***p < 0.001$.

regulates alternative splicing of numerous premRNA transcripts. Moreover, nuclear HuR regulates neurogenesis through modulating the FAK premRNA splicing switch. Taken together, these data suggest that the functional role of cytoplasmic or nuclear HuR could be cell type specific.

Ciliogenesis is a complex sequence of events involving the generation and docking of BBs at the apical membrane, followed by ciliary axoneme generation (Ishikawa and Marshall, 2011). *HuR* cKO mice had fewer cilia tufts and ciliary BB than WT mice. Moreover, some BBs failed to localized apically and dock at the apical membrane in HuR-deficient ependymal cells, while the typical 9 + 0 ring microtubule triplets of BBs and the 9 + 2 ring microtubule doublets of motile cilium were comparable in both WT and cKO ependymal cells. These data suggest that HuR deficiency likely impairs the apical docking of BBs and subsequently leads to attenuated ciliogensis, but not ciliary movement in ependymal cells. In addition, ciliogenesis requires a complex program of macromolecular synthesis and assembly, which must be properly regulated (Ishikawa and Marshall, 2011). Particularly, cilium-specific and flagellum-specific proteins play important roles in assembly and function of mammalian cilia and their deficiency results in the pediatric syndrome primary ciliary dyskinesis (PCD), including hydrocephalus. Among them, Cfap52 expression is correlated with the presence of motile cilia, indicating Cfap52 is a marker for motile cilia-bearing cells (Hirschner et al., 2007). A homozygous Cfap52 deletion has been found in patients with laterality disorder (Ta-Shma et al., 2015). Depletion of Cfap52 in zebrafish caused hydrocephalus, however, ciliary movement remained intact (Hirschner et al., 2007). HuR deficiency results in few cilia bundles in ependymal cells but does not affect the CBF. Mechanistically, HuR binds to *Cfap52* mRNA and loss of HuR leads to accelerate its mRNA degradation, suggesting that HuR-Cfap52 regulatory axis is required for ciliogenesis and its dysregulation contributes to the pathogenesis of hydrocephalus.

The forkhead family transcription factor Foxj-1 and Rfx-3 are two key transcriptional regulators required for the differentiation of motile ciliated cells and ciliogenesis (Baas et al., 2006; Jacquet et al., 2009). Target gene analyses revealed that Cfap52 is the effector gene of Foxj-1 and Rfx factors (Newton et al., 2012; Lemeille et al., 2020). In our study, however, we found that HuR deficiency did not affect the expression of Foxj-1 and Rfx-3. As a HuR target mRNA, *Cfap52* mRNA decay was accelerated, thereby led to decrease its mRNA expression in HuR-deficient ependymal cells. Furthermore, we found that knock-down of Cfap52 expression resulted in defective development of ependymal cells with few cilia. While overexpression of Cfap52 was able to rescue the defective development of ependymal cells caused by HuR-deficiency. Therefore, beyond the transcriptional
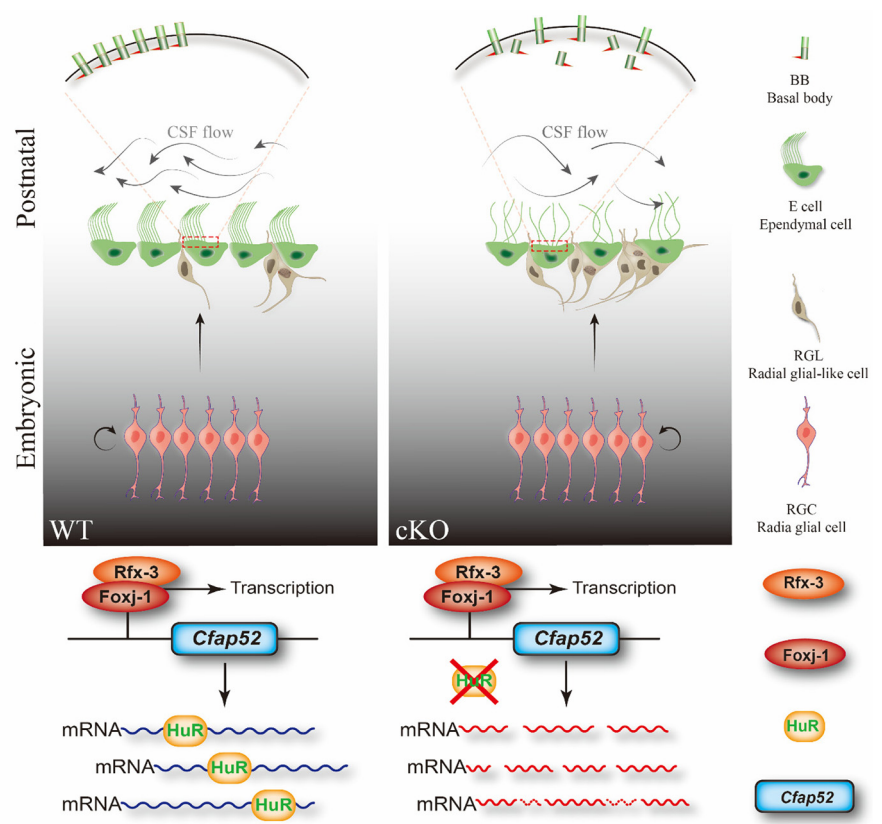
Figure 14. Working model illustrating that HuR regulates ependymal cell development through stabilizing *Cfap52* mRNA.

regulation by Foxj-1 and Rfx factors, our data suggest that HuR-involved posttranscriptional regulation on *Cfap52* mRNA is essential to fulfil ependymal cell development.

References

Baas D, Meiniel A, Benadiba C, Bonnafe E, Meiniel O, Reith W, Durand B (2006) A deficiency in RFX3 causes hydrocephalus associated with abnormal differentiation of ependymal cells. Eur J Neurosci 24:1020–1030.

Casey AT, Kimmings EJ, Kleinlugtebeld AD, Taylor WA, Harkness WF, Hayward RD (1997) The long-term outlook for hydrocephalus in childhood. A ten-year cohort study of 155 patients. Pediatr Neurosurg 27:63–70.

Chen CY, Ezzeddine N, Shyu AB (2008) Messenger RNA half-life measurements in mammalian cells. Methods Enzymol 448:335–357.

Dawe HR, Farr H, Gull K (2007) Centriole/basal body morphogenesis and migration during ciliogenesis in animal cells. J Cell Sci 120:7–15.

Del Bigio MR (2010) Ependymal cells: biology and pathology. Acta Neuropathol 119:55–73.

Delgehyr N, Meunier A, Faucourt M, Bosch Grau M, Strehl L, Janke C, Spassky N (2015) Ependymal cell differentiation, from monociliated to multiciliated cells. Methods Cell Biol 127:19–35.

Fan XC, Steitz JA (1998) HNS, a nuclear-cytoplasmic shuttling sequence in HuR. Proc Natl Acad Sci USA 95:15293–15298.

Furey CG, Choi J, Jin SC, Zeng X, Timberlake AT, Nelson-Williams C, Mansuri MS, Lu Q, Duran D, Panchagnula S, Allocco A, Karimy JK, Khanna A, Gaillard JR, DeSpenza T, Antwi P, Loring E, Butler WE, Smith ER, Warf BC, et al. (2018) De novo mutation in genes regulating neural stem cell fate in human congenital hydrocephalus. Neuron 99:302–314.e4.

Ghosh M, Aguila HL, Michaud J, Ai Y, Wu MT, Hemmes A, Ristimaki A, Guo C, Furneaux H, Hla T (2009) Essential role of the RNA-binding protein HuR in progenitor cell survival in mice. J Clin Invest 119:3530–3543.

Guerra MM, Henzi R, Ortloff A, Lichtin N, Vío K, Jiménez AJ, Dominguez-Pinos MD, González C, Jara MC, Hinostroza F, Rodríguez S, Jara M,

Ortega E, Guerra F, Sival DA, den Dunnen WFA, Pérez-Fígares JM, McAllister JP, Johanson CE, Rodríguez EM (2015) Cell junction pathology of neural stem cells is associated with ventricular zone disruption, hydrocephalus, and abnormal neurogenesis. J Neuropathol Exp Neurol 74:653–671.

Guirao B, Meunier A, Mortaud S, Aguilar A, Corsi J-M, Strehl L, Hirota Y, Desoeuvre A, Boutin C, Han YG, Mirzadeh Z, Cremer H, Montcouquiol M, Sawamoto K, Spassky N (2010) Coupling between hydrodynamic forces and planar cell polarity orients mammalian motile cilia. Nat Cell Biol 12:341–350.

Hirschner W, Pogoda HM, Kramer C, Thiess U, Hamprecht B, Wiesmüller KH, Lautner M, Verleysdonk S (2007) Biosynthesis of Wdr16, a marker protein for kinocilia-bearing cells, starts at the time of kinocilia formation in rat, and wdr16 gene knockdown causes hydrocephalus in zebrafish. J Neurochem 101:274–288.

Huh MS, Todd MA, Picketts DJ (2009) SCO-ping out the mechanisms underlying the etiology of hydrocephalus. Physiology (Bethesda) 24:117–126.

Ibanez-Tallon I, Heintz N, Omran H (2003) To beat or not to beat: roles of cilia in development and disease. Hum Mol Genet 12:R27–R35.

Ishikawa H, Marshall WF (2011) Ciliogenesis: building the cell's antenna. Nat Rev Mol Cell Biol 12:222–234.

Jacquet BV, Salinas-Mondragon R, Liang H, Therit B, Buie JD, Dykstra M, Campbell K, Ostrowski LE, Brody SL, Ghashghaei HT (2009) FoxJ1-dependent gene expression is required for differentiation of radial glia into ependymal cells and a subset of astrocytes in the postnatal brain. Development 136:4021–4031.

Kahle KT, Kulkarni AV, Limbrick DD Jr, Warf BC (2016) Hydrocephalus in children. Lancet 387:788–799.

Kousi M, Katsanis N (2016) The genetic basis of hydrocephalus. Annu Rev Neurosci 39:409–435.

Lemeille S, Paschaki M, Baas D, Morlé L, Duteyrat J-L, Ait-Lounis A, Barras E, Soulavie F, Jerber J, Thomas J, Zhang Y, Holtzman MJ, Kistler WS, Reith W, Durand B (2020) Interplay of RFX transcription factors 1, 2 and 3 in motile ciliogenesis. Nucleic Acids Res 48:9019–9036.

Marshall WF (2008) The cell biological basis of ciliary disease. J Cell Biol 180:17–21.

Matsuo M, Shimada A, Koshida S, Saga Y, Takeda H (2013) The establishment of rotational polarity in the airway and ependymal cilia: analysis with a novel cilium motility mutant mouse. Am J Physiol Lung Cell Mol Physiol 304:L736–L745.

McAllister JP 2nd (2012) Pathophysiology of congenital and neonatal hydrocephalus. Semin Fetal Neonatal Med 17:285–294.

Mirzadeh Z, Doetsch F, Sawamoto K, Wichterle H, Alvarez-Buylla A (2010a) The subventricular zone en-face: wholemount staining and ependymal flow. J Vis Exp (39):1938.

Mirzadeh Z, Han YG, Soriano-Navarro M, García-Verdugo JM, Alvarez-Buylla A (2010b) Cilia organize ependymal planar polarity. J Neurosci 30:2600–2610.

Miyan JA, Nabiyouni M, Zendah M (2003) Development of the brain: a vital role for cerebrospinal fluid. Can J Physiol Pharmacol 81:317–328.

Newton FG, zur Lage PI, Karak S, Moore DJ, Göpfert MC, Jarman AP (2012) Forkhead transcription factor Fd3F cooperates with Rfx to regulate a gene expression program for mechanosensory cilia specialization. Dev Cell 22:1221–1233.

Ohata S, Alvarez-Buylla A (2016) Planar organization of multiciliated ependymal (E1) cells in the brain ventricular epithelium. Trends Neurosci 39:543–551.

Pilaz LJ, Silver DL (2015) Post-transcriptional regulation in corticogenesis: how RNA-binding proteins help build the brain. Wiley Interdiscip Rev RNA 6:501–515.

Rouillard AD, Gundersen GW, Fernandez NF, Wang Z, Monteiro CD, McDermott MG, Ma'ayan A (2016) The harmonizome: a collection of processed datasets gathered to serve and mine knowledge about genes and proteins. Database (Oxford) 2016:baw100.

Satir P, Christensen ST (2007) Overview of structure and function of mammalian cilia. Annu Rev Physiol 69:377–400.

Sironen A, Kotaja N, Mulhern H, Wyatt TA, Sisson JH, Pavlik JA, Miiluniemi M, Fleming MD, Lee L (2011) Loss of SPEF2 function in mice results in spermatogenesis defects and primary ciliary dyskinesia. Biol Reprod 85:690–701.

Spassky N, Meunier A (2017) The development and functions of multiciliated epithelia. Nat Rev Mol Cell Biol 18:423–436.

Spassky N, Merkle FT, Flames N, Tramontin AD, García-Verdugo JM, Alvarez-Buylla A (2005) Adult ependymal cells are postmitotic and are derived from radial glial cells during embryogenesis. J Neurosci 25:10–18.

Srikantan S, Gorospe M (2011) UneCLIPsing HuR nuclear function. Mol Cell 43:319–321.

Tang C, Wang M, Wang P, Wang L, Wu Q, Guo W (2019) Neural stem cells behave as a functional niche for the maturation of newborn neurons through the secretion of PTN. Neuron 101:32–44.6.

Ta-Shma A, Perles Z, Yaacov B, Werner M, Frumkin A, Rein AJ, Elpeleg O (2015) A human laterality disorder associated with a homozygous WDR16 deletion. Eur J Hum Genet 23:1262–1265.

Tissir F, Goffinet AM (2013) Shaping the nervous system: role of the core planar cell polarity genes. Nat Rev Neurosci 14:525–535.

Tully HM, Dobyns WB (2014) Infantile hydrocephalus: a review of epidemiology, classification and causes. Eur J Med Genet 57:359–368.

Wallingford JB (2010) Planar cell polarity signaling, cilia and polarized ciliary beating. Curr Opin Cell Biol 22:597–604.

Wang Y, Guo Y, Tang C, Han X, Xu M, Sun J, Zhao Y, Zhang Y, Wang M, Cao X, Zhu X, Guo W (2019) Developmental cytoplasmic-to-nuclear translocation of RNA-binding protein HuR is required for adult neurogenesis. Cell Rep 29:3101–3117.e7.

Yao KM, Samson ML, Reeves R, White K (1993) Gene elav of Drosophila melanogaster: a prototype for neuronal-specific RNA binding protein gene family that is conserved in flies and humans. J Neurobiol 24:723–739.

Zimmerman L, Parr B, Lendahl U, Cunningham M, McKay R, Gavin B, Mann J, Vassileva G, McMahon A (1994) Independent regulatory elements in the nestin gene direct transgene expression to neural stem cells or muscle precursors. Neuron 12:11–24.